JGR Space Physics

RESEARCH ARTICLE
10.1029/2019JA027062

Kinetic Alfvén Waves From Magnetotail to the Ionosphere in Global Hybrid Simulation Associated With Fast Flows

Lei Cheng[1], Yu Lin[1], J. D. Perez[1], Jay R. Johnson[2], and Xueyi Wang[1]

[1]Department of Physics, Auburn University, Auburn, AL, USA, [2]Department of Engineering and Computer Science, Andrews University, Berrien Springs, MI, USA

Key Points:
- Global evolution of kinetic Alfvén waves (KAWs) from the magnetotail to the ionosphere is analyzed using a 3-D global hybrid simulation
- KAWs are shown to be generated in the plasma sheet by reconnection and in the flow-braking region due to ion inertial effect
- Dipole-like field region alters the structure and strength of the shear Alfvén waves that propagate to the ionosphere

Supporting Information:
- Supporting Information S1
- Movie S1
- Movie S2

Correspondence to:
L. Cheng,
lzc0025@auburn.edu

Citation:
Cheng, L., Lin, Y., Perez, J. D., Johnson, J. R., & Wang, X. (2020). Kinetic Alfvén waves from magnetotail to the ionosphere in global hybrid simulation associated with fast flows. *Journal of Geophysical Research: Space Physics, 125*, e2019JA027062. https://doi.org/10.1029/2019JA027062

Received 22 JUN 2019
Accepted 1 NOV 2019
Accepted article online 29 JAN 2020

Abstract We have used the Auburn Global Hybrid Code in 3-D to study the generation, dynamics, and global structure of kinetic Alfvén waves (KAWs) from the magnetotail to the ionosphere. Our results show that KAWs are generated in magnetic reconnection in the plasma sheet, located around fast flows, and carrying transverse electromagnetic perturbations, parallel Poynting fluxes, parallel currents, and parallel electric field. Overall, shear Alfvénic turbulent spectrum is found in the plasma sheet. The KAWs are shear Alfvén waves possessing short perpendicular wavelength with $k_\perp \rho_i \sim 1$, where $k_\perp$ is the perpendicular wave number and ρ_i the ion Larmor radius. The KAWs are identified by their dispersion relation and polarizations. The structures of these KAWs embedded in the plasma sheet are also revealed by placing a virtual satellite in the tail. In order to understand whether the Poynting fluxes carried by the shear Alfvén waves/KAWs in the plasma sheet can be carried directly along field lines to the ionosphere, we have tracked the wave propagation from the plasma sheet to the ionosphere. It is found that in front of the flow-braking region, the structure and strength of the shear Alfvén waves are significantly altered due to interaction with the dipole-like field, mainly by the flow shear associated with the azimuthal convection. Also in front of the dipole-like field region, ion kinetic effects (Hall effects) lead to the generation of additional pairs of KAWs. As such, the generation and transport of the shear Alfvén waves/KAWs to the ionosphere are illustrated for the first time in a comprehensive manner on the global scale.

1. Introduction

A magnetospheric substorm is a disturbance of the magnetosphere that causes energy in the magnetotail to be released and injected into the high-latitude ionosphere. Near-Earth magnetic reconnection in the magnetotail is thought to trigger magnetospheric substorms onset (Angelopoulos et al., 2008), although the underlying mechanism is not fully resolved (Lui, 2009). Bursty bulk flows (BBFs; Angelopoulos et al., 1994), which are temporally and spatially localized high-speed streams of the plasma in the tail, are found to be an important dynamical consequence of magnetic reconnection, a process resulting in the changing of magnetic topology and release of magnetic energy. Magnetic flux ropes and dipolarization fronts, referring to the alteration of magnetic field configuration from stretched to more dipolarized form, are the most notable structures associated with BBFs.

Shear Alfvén waves are fundamental and ubiquitous plasma waves (Anderson et al., 1982; Chaston et al., 1999; Greenwald & Walker, 1980) carrying transverse electromagnetic perturbations and thus field-aligned currents. While localized structures associated with the fast flows, for example, dipolarization fronts, entropy bubbles, and flow vorticies, have also been suggested for the generation of field-aligned currents in the tail (Keiling et al., 2009; Sun et al., 2013), shear Alfvénic perturbations are a coherent normal mode that can carry the field-aligned currents globally. When the perpendicular (to the magnetic field) wavelength is short and comparable to the ion gyroradius, parallel electric fields $E_\parallel$ can be developed, in the shear Alfvén waves, which facilitate particle heating, acceleration, and transport. Kinetic Alfvén waves (KAWs) are shear Alfvén waves with small perpendicular wavelength comparable to the ion gyroradius or the electron inertial length, that is, $k_\perp \rho_i \sim 1$, where $k_\perp$ is the perpendicular wave number and ρ_i the ion Larmor radius. During substorms, shear Alfvénic fluctuations, including KAWs, are found in many observations (Dubinin et al., 1990; Keiling, 2009; Keiling et al., 2000; Osaki et al., 1998; Takahashi et al., 1988; Wygant et al., 2000, 2002). KAWs have been found in the plasma sheet associated with fast flows (Angelopoulos et al., 2002; Chaston et al., 2009, 2012), at the plasma sheet boundary layer (PSBL; Gershman et al., 2017; Wygant et al., 2002), and in the inner magnetosphere (Chaston et al., 2006, 2014; Huang et al., 1997). It has been argued that

the KAWs observed around the tail plasma sheet carry sufficient Poynting flux flowing along magnetic field lines toward the ionosphere to power low-altitude auroral acceleration (Angelopoulos et al., 2002; Lessard et al., 2011).

Shear Alfvén waves in the kinetic regime differ from those in an magnetohydrodynamic (MHD) treatment because the short wavelength requires a significant parallel electric field to maintain charge neutrality because of ion density perturbations caused by the ion polarization drift. When the electron thermal speed is higher than the Alfvén speed, the parallel electric field counteracts electron pressure (which would push the electrons away from the ion density perturbations; Hasegawa, 1976). When the electron thermal speed is lower than the Alfvén speed, the electric field must overcome the electron inertia (which prevents the electrons from responding rapidly to the ion density perturbations; Goertz & Boswell, 1979). Hasegawa (1976) first suggested that the parallel electric fields associated with small-scale KAWs could efficiently accelerate particles on magnetic field lines. KAWs were further suggested as a mechanism that gives rise to particle acceleration on auroral field lines (Goertz, 1984) as well as transverse ion heating in that region (Temerin & Roth, 1986). Chaston et al. (2009) presented observations in the magnetotail from the Cluster spacecraft showing that KAWs radiate outward from the X line with outward energy fluxes equivalent to that contained in the outstreaming ions. Wave-particle energy exchange has been confirmed between KAWs and plasma particles near the dayside magnetopause by high-resolution Magnetospheric Multiscale (MMS) mission observations (Gershman et al., 2017). Thus, KAWs can be an important mechanism in plasma transport, plasma heating, and particle acceleration (Chaston et al., 2007; Hasegawa & Chen, 1976).

The basic properties of KAWs are described by their dispersion relation. While MHD Alfvén waves satisfy the relation $\omega = k_\parallel V_A$, the dispersion relation of KAWs can be written as

$$\omega^2 = k_\parallel^2 V_A^2 \left[1/\left(1-\Gamma_0\left(k_\perp^2\rho_i^2\right)e^{-k_\perp^2\rho_i^2}\right) + T_e/T_i\right] k_\perp^2\rho_i^2, \tag{1}$$

where ω is the ion gyrofrequency, $k_\parallel$ is the wave number parallel to the background magnetic field, V_A is the Alfvén speed, Γ_0 is the full Bessel function, ρ_i is the ion gyroradius, and T_e and T_i are the electron and ion temperatures, respectively. Employing a Padé approximation $\Gamma_0(k_\perp^2\rho_i^2)e^{-k_\perp^2\rho_i^2} \approx 1/(1+k_\perp^2\rho_i^2)$, the relation can be simplified to

$$\omega^2 = k_\parallel^2 V_A^2[1+(1+T_e/T_i)k_\perp^2\rho_i^2] = k_\parallel^2 V_A^2[1+k_\perp^2(\rho_i^2+\rho_s^2)], \tag{2}$$

where $\rho_s = (T_e/m_i)^{\frac{1}{2}}/\Omega_i$, with Ω_i being the ion cyclotron frequency (Johnson & Cheng, 1997). Since shear Alfvén waves possess transverse polarizations in both the electric and magnetic fields, the polarization relation of KAWs can be expressed as

$$\left|\delta E_\perp/\delta B_\perp\right| = V_A\left(1+k_\perp^2\rho_i^2\right)\left[1+k_\perp^2(\rho_i^2+\rho_s^2)\right]^{-1/2}, \tag{3}$$

where $\delta E_\perp$ is the perturbed electric field in the direction of $k_\perp$ and $\delta B_\perp$ is the perturbed magnetic field, which is perpendicular to both the background magnetic field and $\delta E_\perp$. The parallel electric field of KAWs can be expressed as (Johnson & Cheng, 1997; Keiling, 2009; Lysak & Lotko, 1996)

$$\left|\delta E_\parallel/\delta E_\perp\right| = k_\parallel k_\perp\rho_s^2/(1+k_\perp^2\rho_i^2). \tag{4}$$

Shear Alfvén waves can also be identified by the Walén relation, which describes the relationship between fluctuations of velocity and magnetic field (Barnes & Hollweg, 1974; Belcher et al., 1969; Hudson, 1971; Walén, 1944). In the MHD description with ion temperature anisotropy, the Walén relation in the de Hoffmann-Teller frame, in which the convection electric field is zero, can be written as

$$\delta\mathbf{V} = \pm\xi^{1/2}\delta\mathbf{V}_A, \tag{5}$$

where $\delta\mathbf{V}$ is the plasma velocity in the Hoffmann-Teller frame, $\delta\mathbf{V}_A = \delta\mathbf{B}/\sqrt{\mu_0\rho}$ is the fluctuation of magnetic field in the form of the Alfvén speed, $\xi = 1-\mu_0\frac{P_\parallel - P_\perp}{B^2}$ is the thermal anisotropic parameter, and the $+(-)$ sign corresponds to $k_\parallel < 0\,(>0)$. Nevertheless, the Walén relation is modified when including the particle kinetic effects. Based on the kinetic-fluid model (Cheng & Johnson, 1999; Damiano et al., 2015, 2019), the Walén relation of KAWs (see Appendix A for derivation) is given by

$$\delta\mathbf{V}_i \approx \pm\delta\mathbf{V}_A\left(\frac{1+k_\perp^2\lambda_e^2}{1+\left(1+\frac{T_e}{T_i}\right)k_\perp^2\rho_i^2}\right)^{1/2}\left(\frac{1}{1+1.25k_\perp^2\rho_i^2}\right), \tag{6}$$

where λ_e is electron skin depth. Note that equation (6) is valid either the inertial Alfvén wave or the KAW with ion acoustic (hot electron) and/or ion gyroradius effects. Dropping $k_\perp \lambda_e$ for KAWs in the outer magnetosphere, the Walén relation of KAWs in hybrid model can be simplified as

$$\delta \mathbf{V}_i \approx \pm \delta \mathbf{V}_A \left(\frac{1}{\sqrt{1+\left(1+\frac{T_e}{T_i}\right)k_\perp^2 \rho_i^2}} \right) \left(\frac{1}{1+1.25 k_\perp^2 \rho_i^2} \right). \tag{7}$$

Although KAWs have been observed in the magnetotail and ionosphere, their generation mechanisms and global transport properties are still unclear. Previous theories and simulations have shown that KAWs can be generated via various mechanisms such as magnetic reconnection (Liang et al., 2016, 2017; Shay et al., 2011), mode conversion (Hasegawa & Chen, 1976; Johnson & Cheng, 1997), and phase mixing (Guo et al., 2015; Hasegawa, 1976; Vásconez et al., 2015). Shay et al. (2011) have shown the signature of KAWs generated by reconnection via a 2-D particle-in-cell code. Liang et al. (2016, 2017) have presented a 3-D hybrid simulation in a Harris current sheet showing that KAWs are found throughout the transient plasma bulge region and propagate outward along field lines with a slightly super-Alfvénic velocity. Dai et al. (2017) suggested KAW eigenmode (Dai, 2009) as an explanation of Hall fields and currents in the process of magnetic reconnection. Mode conversion from compressional waves to KAWs under various solar wind conditions at the dayside magnetopause has been studied using hybrid simulations (Lin et al., 2010, 2012; Shi et al., 2013, 2017). KAWs can also be generated by large-scale phase mixing of MHD shear Alfvén waves.

Since the magnetotail contains multiple plasma boundary layers embedded in and coupled with the global dynamics, multiple boundary layers exist in the highly nonuniform plasma and magnetic field. Questions remain. Will KAWs be generated at those boundaries? What will happen when Alfvén waves interact with the boundaries during their propagation? The generation and evolution of KAWs in the global system are still far from being understood.

In this paper, we investigate the generation and evolution of KAWs in the magnetotail associated with magnetotail reconnection and fast flows by using a 3-D global hybrid code, which solves the fully kinetic ion physics in the self-consistent electromagnetic field. KAWs are found to be generated by near-Earth magnetic reconnection. In addition, KAWs are also identified in the flow-braking region, and the role of the flow-braking region in the propagation of KAWs and the associated Poynting flux from the tail to the ionosphere is illustrated. The subsequent impacts of the tail fast flows to the inner magnetosphere (e.g., Lysak et al., 2015) is not the focus of this paper.

The paper is organized as follows. Section 2 describes the simulation model. Then, the simulation results are shown in section 3. Finally, section 4 presents a summary and discussion.

2. Simulation Model

The simulation tool used in this paper is the Auburn Global Hybrid Code in 3-D (Lin et al., 2014, 2017), a 3-D global hybrid code including both the dayside and nightside magnetosphere. In this code, ions (protons) are treated as fully kinetic particles, while electrons are treated as a massless fluid. The simulation domain extends from $x = -60R_E$ on the nightside to $x = +20R_E$ on the dayside, $y = -30R_E$ to $+30R_E$ in the dawn-dusk direction, and $z = -30R_E$ to $+30R_E$ in the north-south direction in the GSM and Cartesian coordinate system. There are six outer boundaries. The fixed solar wind and interplanetary magnetic field (IMF) conditions are imposed at $x = +20R_E$, while the free boundary conditions are used at the other five boundaries. The inner boundary is located at $r = 3.5R_E$, where a magnetospheric-ionospheric electrostatic coupling model is employed. The field-aligned currents, mapped along the geomagnetic field lines from the inner boundary into the ionosphere, are the input to the ionospheric potential equation (Raeder et al., 1995),

$$\nabla \cdot (-\bar{\Sigma} \cdot \nabla \Phi) = J_\parallel \sin I, \tag{8}$$

where $\bar{\Sigma}$ is the conductance tensor, Φ is the electric potential, $J_\parallel$ is the field-aligned current density, and I is the inclination of the dipole field at the ionosphere. Uniform Pederson conductance $\Sigma_P = 5$ Siemens is

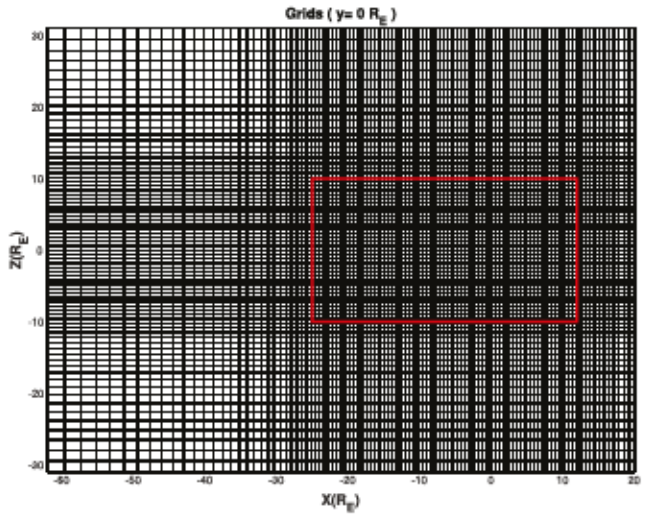

Figure 1. Configuration of the grid used in the simulation. The red rectangle denotes the region with grid size: $(\Delta x, \Delta y, \Delta z) = (0.15, 0.15, 0.15)R_E$.

adopted, while the Hall conductance Σ_H is assumed to be zero. The details about the boundary conditions can be seen in Lin et al. (2014). The equation for ion particle motion, in the simulation units, is written as

$$\frac{d\mathbf{v}_p}{dt} = \mathbf{E} + \mathbf{v}_p \times \mathbf{B} - \nu(\mathbf{V}_p - \mathbf{V}_e), \tag{9}$$

where $\mathbf{v}_p$ is the ion particle velocity, ν is an ad hoc current-dependent collision frequency with typical peak collision frequency ~0.01–0.1 Ω_i (Tan et al., 2011) used to model the anomalous resistivity, and $\mathbf{V}_p$ and $\mathbf{V}_e$ are the bulk flow velocities of ions and electrons, respectively. A cold, incompressible ion fluid coexists with particle ions (Lin & Wang, 2005; Swift, 1996) in the inner magnetosphere ($r < 6.5 \quad R_E$), considering this simulation revolves the ion kinetic physics in the outer magnetosphere. The number density of the cold ion fluid is assumed to be $N_f = (N_{eq}/r^3)[1 - \tanh(r - 6.5)]$, where $N_{eq} = 1{,}000\ \mathrm{cm}^{-3}$. The electron flow speed is calculated from Ampere's law,

$$\mathbf{V}_e = \mathbf{V}_i - \frac{\nabla \times \mathbf{B}}{\alpha N}, \tag{10}$$

where $\alpha = (\mu_0 e^2/m_i)$, μ_0 is the permeability of free space, e is the electron charge, and m_i is the ion mass. The ion inertial length d_i is set as $d_i = 1/\sqrt{(\alpha N)}$.

The massless electron momentum equation is given as

$$\mathbf{E} = -\mathbf{V}_e \times \mathbf{B} - 1/(N)\nabla p_e - \nu(\mathbf{V}_e - \mathbf{V}_i), \tag{11}$$

where $N = N_p + N_f$ is the total ion number density with N_p and N_f being the number densities of discrete ions and cold ion fluid, respectively. $\mathbf{V}_i = (N_p/N)\mathbf{V}_p + (N_f/N)\mathbf{V}_f$ is the total ion bulk flow velocity, with $\mathbf{V}_f$ being the flow velocity of the cold ion flow. Note that $\nabla p_e = T_e \nabla N$ since the electron fluid is assumed to be isothermal with a constant temperature T_e. The magnetic field is advanced in time by Faraday's law,

$$\frac{\partial \mathbf{B}}{\partial t} = -\nabla \times \mathbf{E}. \tag{12}$$

In the case presented, a purely southward IMF is chosen, with the field strength $B_0 = 10$ nT and ion number density $N_0 = 6\ \mathrm{cm}^{-3}$, corresponding to a solar wind ion gyrofrequency $\Omega_0 = 0.958\mathrm{s}^{-1}$. The solar wind ion inertial length $d_{i0} = c/\omega_{pi0}$ is set as $0.1R_E$, where ω_{pi0} is the plasma frequency of solar wind and c is the light speed. Nonuniform cell grids are used, with a grid size of $(\Delta x, \Delta y, \Delta z) = (0.15, 0.15, 0.15)R_E$ in the near-Earth regions with $-25R_E \le x \le 12 \quad R_E$, $-12R_E \le y \le 12R_E$, and $-10 \quad R_E \le z \le 10R_E$ and a lower resolution in other regions. The cell dimensions are set as $n_x \times n_y \times n_z = 337 \times 241 \times 217$. The configuration of the grid is shown in Figure 1. A total of 2×10^9 particles are used. A typical particle time step interval is $\Delta t = 0.05\Omega_0^{-1}$. Note that the hybrid model is valid for low-frequency ion kinetic physics with $\omega \sim \Omega_i$ and $k\rho_i \sim 1$ (Lin et al., 2014). Given that the peak ion number density in the plasma sheet is on the order of 0.33 N_0 and $d_i = \sqrt{\frac{N_0}{N_i}} d_{i0}$, the lowest ion inertial length in the magnetotail is around $0.17R_E$ in the simulation. Therefore, the grid size, $(\Delta x, \Delta y, \Delta z) = (0.15, 0.15, 0.15)R_E$, is small enough to resolve the ion kinetic physics.

It is necessary to scale the kinetic effects in order to compare with typical values in the magnetosphere (Lin & Wang, 2005; Lin et al., 2014; Swift, 1996), since an artificial solar wind ion inertial length is adopted given the finite computing resources. The time scale presented in the simulation is increased by a factor of 6.76 in order to compare with typical values in the magnetosphere. The factor is chosen because the artificial solar wind ion inertial length ($0.1R_E$) used in the simulation is 6.76 times as large as the realistic one ($0.0148R_E$) for a typical solar wind density of 6 cm^{-3}. Thus, the convection speed is faster in the simulation since the positions of the bow shock and magnetopause are assumed to be realistic.

In the presentation that follows as shown in Table 1, the spatial length (L) is in units of $\mathrm{R_E}$ and the time (t) in units of seconds. The magnetic field (B) is in units of nT and the temperature (T) in units of eV. The electric field (E) is in units of V/m and the current density (J) in units of $\mu\mathrm{A/m}^2$. The velocity (V) is in km/s and the Poynting flux (S) in units of $\mathrm{W/m}^2$. The ion number density (N) is in units of cm^{-3} as scaled to the realistic ion inertial length.

Table 1
Units of Parameters

L	t	B	N	E	J	T	V	S
R_E	s	nT	cm^{-3}	V/m	nA/m^2	eV	km/s	W/m^2

3. Simulation Results

3.1. Global View

The results of the simulation described in this paper have the following input parameters: IMF components $B_{x0} = B_{y0} = 0$, and $B_{z0} = -10$ nT, Alfvén Mach number $M_A = 7.87$, ion density $N_0 = 6$ cm^{-3}, convection speed $V_0 = 700$ km/s, ion temperature $T_{i0} = 10$ eV, and electron-to-ion temperature ratio $T_{e0}/T_{i0} = 2$ in the solar wind. Runs with various Mach numbers are also conducted, and the generation of fast flows and Alfvén waves are found to be similar for $M_A = 4 - 8$, although their strengths vary. The electron-to-ion temperature ratio in the solar wind is set to 2 so that the ratio in the plasma sheet is realistic. This is necessary because electrons are assumed to be isothermal for simplicity in this simulation and thus not to be heated in the magnetosheath as under the real condition.

Figure 2 shows a time sequence of global views of the magnetic field and ion density in the GSM equator along with typical magnetic field lines. The sequence begins approximately 4 min after the magnetotail forms in the simulation and spans a period of approximately 3 min. The black cones show the ion bulk flow velocity. Open field lines are marked as blue lines, while closed field lines are marked as orange lines. The red lines are dipole magnetic field lines, and the black lines are reconnected magnetic field lines due to the dayside magnetic reconnection at the magnetopause. The initial condition of magnetic field was set as a dipole magnetic field plus mirror dipole magnetic field for $x < 15R_E$ at $t = 0$ s, and the uniform solar wind and IMF occupy the region of $x > 15R_E$. Initially, the ion particle density is $0.05N_0$ in the region of dipole magnetic field. As time proceeds, the magnetosphere forms self-consistently while the solar wind continuously enters the domain and interacts with the dipole magnetic field. The standoff distances of the magnetopause and bow shock are around $8R_E$ and $12R_E$, respectively, as shown in Figure 2a. Magnetic reconnection occurs at the dayside magnetopause around $x = 8R_E$ along X lines through the subsolar point and another in the nightside plasma sheet, which extends from $x = -35R_E$ to $x = -15R_E$. Flux ropes, that is, twisted magnetic field lines, as a signature of magnetic reconnection are shown both at the dayside magnetopause and in the tail plasma sheet. They are marked in Figure 2a as the black field lines at the magnetopause around $x = 8R_E$ and as the violet field lines in the magnetotail plasma sheet around $x = -25R_E$. Significant variations of magnetic field strength and ion number density at the equator in both the magnetotail and magnetosheath are shown in the left- and right-hand columns, respectively, as indicated by the color bars at the bottom of the figure.

The near-tail X line initially developed at $x \approx -25R_E$. In Figure 2a, two typical flux ropes marked as "A" (closed field lines on both sides) and "B" (one side is open, and the other side is closed) are generated by magnetic reconnection at $t = 2391$ s. As shown in the expanded views pointed to by the white arrows, flux rope "A" has both ends of the field line extending sunward (earthward), while flux rope "B" has one end going sunward and the other end extending tailward. At this time flux rope "A" near $x = -22.0R_E$, $y = -6.0R_E$ is moving with earthward fast flows at a speed of a few hundred kilometers per second generated by reconnection, while flux rope "B" near $x = -27.0R_E$, $y = 7.5R_E$ is moving tailward. The two flux ropes also drifted dawnward as shown in Figure 2b as the result of $\mathbf{E} \times \mathbf{B}$ drift associated with Hall electric field (Lin et al., 2014; Lu et al., 2015), which cannot be described by MHD models. A little more than 1 min later, flux rope "A" has drifted sunward and dawnward to $x = -14.5R_E$, $y = -9.0R_E$, and flux rope "B" has drifted antisunward (tailward) and dawnward to $x = -31.0R_E$, $y = 4.0R_E$. A new flux rope with both ends of the field line extending antisunward, marked as "C," is generated at $t = 2{,}470$ s. About 1.5 min later, as shown in Figure 2c, flux rope "B" has continued its eastward drift and moved from the duskside to the dawnside. By this time, flux rope "A" has arrived at the dipole-like field region, where it releases its helicity and merges with the dipole-like magnetic field lines. Once it is deeper in the magnetosphere, it is expected to drift to the duskside due to the magnetic gradient and curvature drift (Lin et al., 2014).

In order to resolve the small structures in the near-Earth magnetotail, Figure 3 provides zoom-in contours of the ion number density (N) and parallel current density ($J_\parallel$) in the equatorial plane from $x = 0R_E$ to $x = -30R_E$ at the same time as in Figure 2a. Earthward fast flows (i.e., BBFs) and tailward fast flow channels

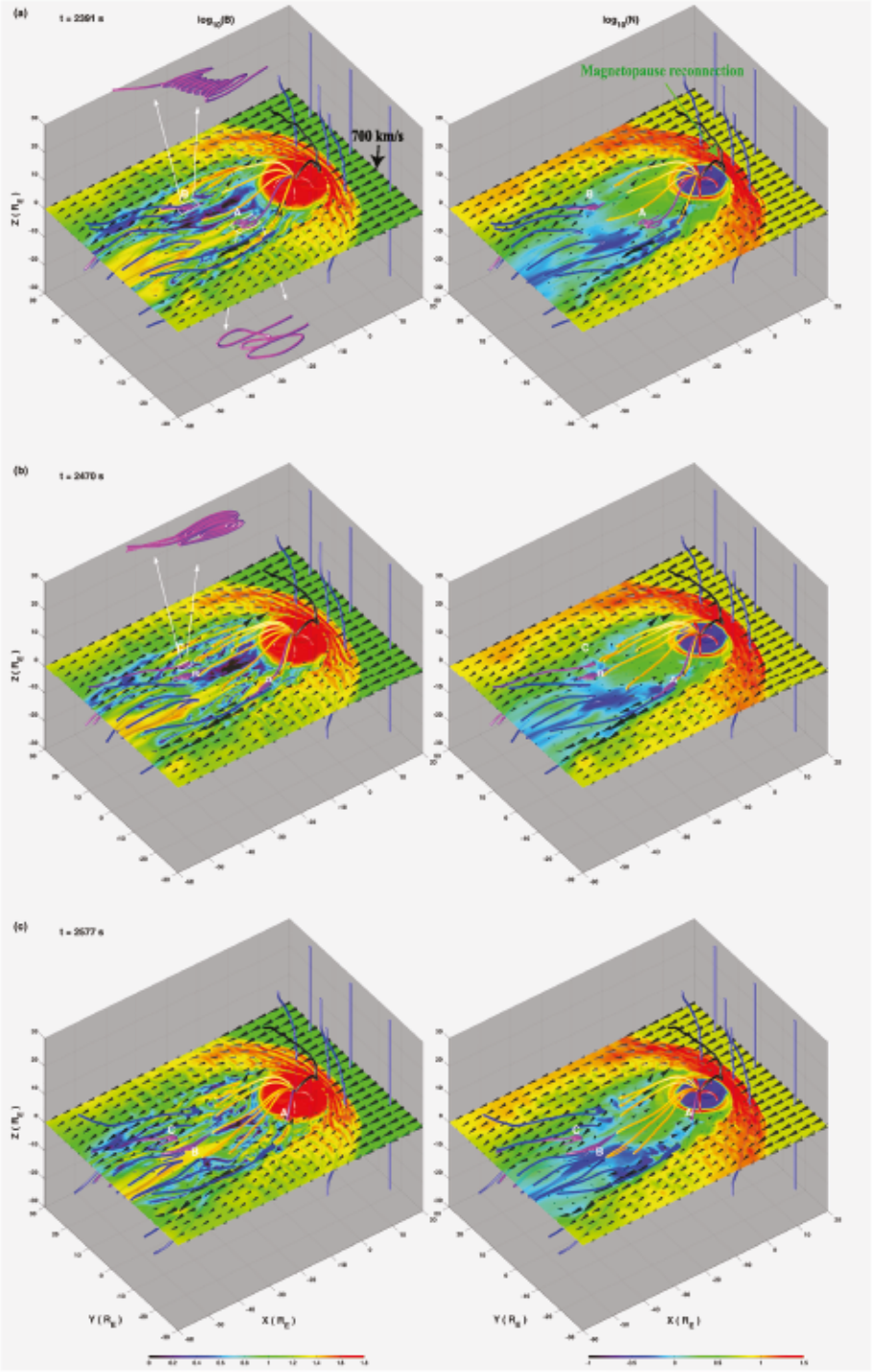

Figure 2. Time variation of contours of B (left column) and N (right column) at the equatorial plane with typical magnetic field lines showing the dayside and nightside magnetosphere, with multiple flux ropes in the plasma sheet. The black cones denote ion bulk flow velocity.

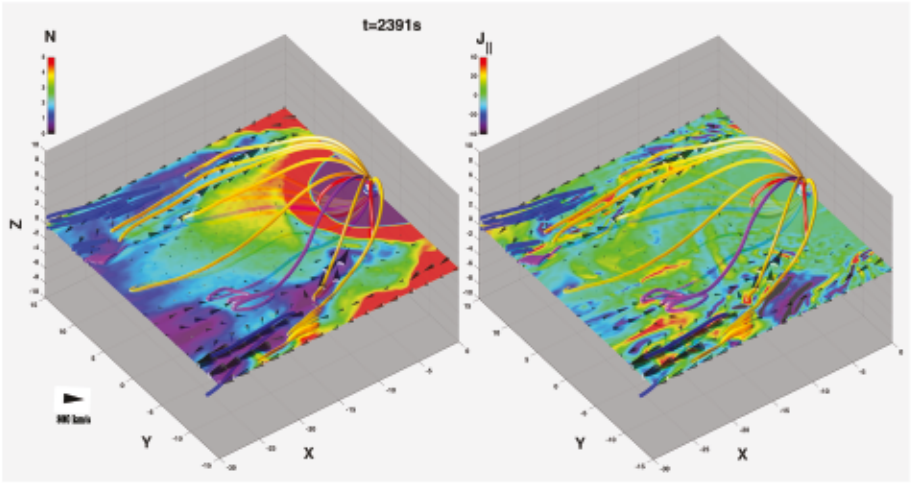

Figure 3. Contours of N and $J_{\|}$ at the equatorial plane with typical magnetic field lines and fast flows at $t = 2{,}469$ s. The black cones denote ion bulk flow velocity.

with speeds of 300–1,000 km/s marked as large black cones are found from $x = -30R_E$ to $x = -10R_E$, sunward and antisunward of the near-tail X line around $x = -25 \quad R_E$, respectively. Enhanced ion density is present inside the flux ropes, which move with the fast flows earthward and tailward. On the earthward side, at the flow-braking region at $r \sim 10R_E$ in front of the strong dipole-like field, the earthward fast flows slow down and convect bidirectionally to the dayside magnetosphere.

During a substorm, many waves are generated by reconnection, including shear Alfvén waves (Chaston et al., 2009; Hong et al., 2008; Lin & Swift, 2002; Sigsbee et al., 2002). In our simulation, near the X line on both the dawnside and duskside around $x = -20R_E$, many small structures of ion number density and parallel current density are shown in the equatorial plane. These kinds of structures are developed on an Alfvén time scale. Since Alfvén waves are a possible carrier of field-aligned currents, we will examine the shear Alfvénic characteristics around the reconnection regions. Note that if these are Alfvén waves, then they are likely to be KAWs because typical MHD Alfvén waves do not have ion density perturbations. This will be confirmed in section 3.2. We will show more information is revealed when the structures of field-aligned current are viewed in the xz plane. Since the xz planes in general show the geometry of the DC magnetic

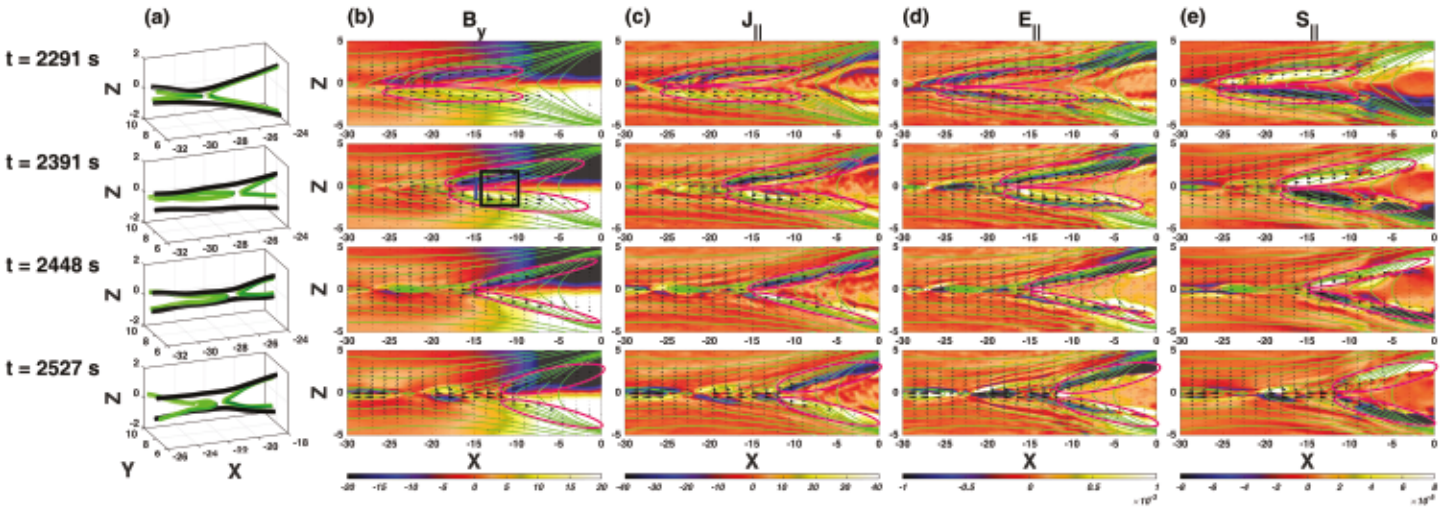

Figure 4. (a) Magnetic field line configuration and contours of (b) transverse magnetic field (B_y), (c) parallel current density ($J_{\|}$), (d) parallel electric field ($E_{\|}$) and (e) parallel Poynting flux ($S_{\|}$) at $t = 2291$s, $t = 2391$s, $t = 2448$s and $t = 2527$s with typical magnetic field fines and ion flow velocity(black arrows) in the plane $y = 8.0R_E$.

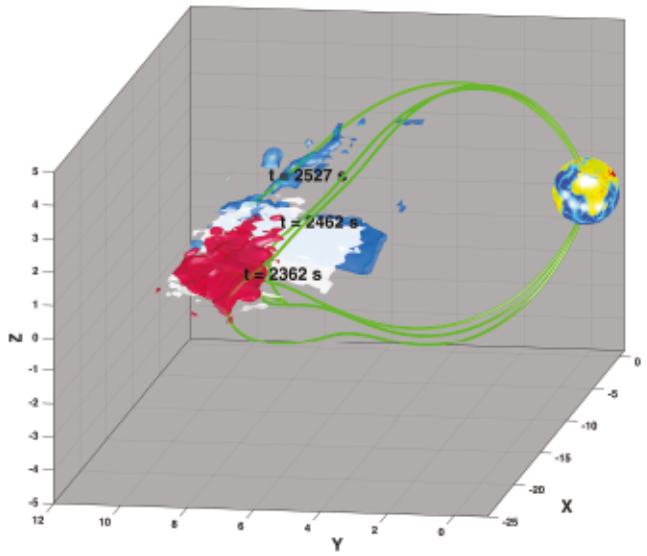

Figure 5. Isosurface plots of $J_{\parallel} = -25$ at $t = 2362$ s (red patch), $t = 2462$ s(white patch) and $t = 2572$ s (blue patch) with typical magnetic field lines (green lines) showing the evolution of the same KAW structure generated around $x = -23$ R_E.

field, the propagation of Alfvén waves can be traced globally from the tail to ionosphere at different local times.

3.2. KAWs in the Magnetotail

Figure 4 shows the time evolution of an X line and contours of parallel current density ($J_{\parallel}$), parallel electric field ($E_{\parallel}$), transverse magnetic field (B_y), and parallel Poynting flux ($S_{\parallel}$) in the xz plane at $y = 8.0R_E$, where reconnection occurs on the duskside in Figure 3. This time evolution begins about 1.5 min before the times shown in Figure 2a and ends about 1 min before the times shown in Figure 2c. At t = 2,291 s, near-Earth magnetic reconnection is found with an X line evident from the configuration of the magnetic field lines at $x = -29$ R_E in Figure 4a. A little more than 1.5 min later, the X line moves a little earthward, located at $x = -27R_E$ at t = 2,391 s. Subsequently, the X line moves a little tailward to $x = -28R_E$ at t = 2,448 s and further to $x = -21$ R_E at t = 2,527 s. The pink circles show the time evolution of the same wave structure generated by reconnection and its propagation to the Earth along magnetic field lines in the plasma sheet boundary layer. The consistent correlation of B_y in Figure 4b, $J_{\parallel}$ in Figure 4c, $E_{\parallel}$ in Figure 4d, and $S_{\parallel}$ in Figure 4e shows these waves have properties of KAWs. The waves have a large perpendicular wave number in the perpendicular direction (roughly z direction). The highly field-aligned extension of these structures indicate $k_{\parallel} \ll k_{\perp}$. The finite parallel Poynting flux inside the pink circle above the equator has the opposite sign compared with that below the equator in Figure 4e. Considering the direction of the local magnetic field lines, the wave structure propagates toward the ionosphere both above and below the equatorial plane. The consistent sign indicates that wave power is absorbed as the wave propagates toward the ionosphere. At the initial time in this sequence, that is, t = 2,291 s, the wavefront at $z = 0.15R_E$ is near $x = -25R_E$. About 100 s later, the wavefront at $z = 0.15$ R_E arrives at $x = -17R_E$. Approximately 1 min later, at t = 2,448 s, the earthward KAWs arrive in the dipole-like field region and then propagate toward the northern and southern ionosphere along the field lines. This is shown by the enhancement of the values of $J_{\parallel}$, $E_{\parallel}$, and B_y at t = 2,527 s (see Movies S1 and S2 included in the supporting information S1 for more details). Note that the background B_y component is much smaller than the transverse perturbation of magnetic field while $x < -12R_E$. So the propagation of KAW structure is nearly in the plane $y = 8.0R_E$. In $x > -12R_E$, the background B_y component cannot be ignored, and the propagation of KAW structure is no longer only in the plane $y = 8.0R_E$. Meantime, a new wave structure arises around $x = -22R_E$ at t = 2527s. The above time scale for the wave propagation is consistent with the Alfvén wave speed, which will be illustrated below.

Figure 5 shows the propagation of KAWs from the magnetotail to the ionosphere in 3-D view, where the red patch, the white patch, and the blue patch mark the same KAW structure at different times. At t = 2,362 s, the highly 3-D structure of KAWs characterized by isosurface of $J_{\parallel}$ marked as the red patch is generated near X lines on the duskside. The structure propagates to the Earth along the magnetic field line and arrives at the dipole-like field region. As time evolves, the structure merges with the Region 1 current on the duskside and propagates to the ionosphere at t = 2,572 s.

In order to further confirm that these waves are KAWs, Figure 6 examines the shear Alfvén polarization relation and Walén relation along the blue line segment (at $x = -15R_E$) marked in the B_y contours in Figure 4 for t = 2,391 s and $y = 8.0R_E$. Figure 6a shows the spectrum of $J_{\parallel}$ in k_x-k_z space, from $x = -15.0$ R_E to $-10.0R_E$ and from $z = -2.0R_E$ to $2.0R_E$ at $y = 8.0R_E$ marked as the black rectangle in Figure 4b. $\mathbf{k}'$ is defined as $\mathbf{k}/2\pi$. Since the background magnetic field is almost in the x direction, with $B \sim B_x$, and the wave number is mainly in the z direction, with $k \sim k_z$ ($k_{\perp} \gg k_{\parallel}$) as shown in Figure 6a, the electric field polarization $\delta E_{\perp}$ and magnetic field polarization $\delta B_{\perp}$ associated with KAWs are predominantly B_y and E_z, respectively. In Figure 6a, k'_z is $0.2 - 0.6/R_E$, and $k_z = 2\pi k'_z \sim 1.3 - 3.8 rad/R_E$. The local ion gyroradius is found to be $\rho_i \sim 0.2$ $R_E - 0.4R_E$. The perpendicular wave number is thus $k_{\perp}\rho_i \sim k_z\rho_i \sim 0.4 - 1.1$ in these waves. Figures 6b and 6c show polarization relation and Walén relation, respectively. The shear Alfvénic transverse components $\delta E_{\perp}$ and $\delta B_{\perp}$ in Figure 6b are well correlated, with $\delta E_{\perp} = -1.17\delta B_{\perp} V_{Ay}$ in $z > 0$ and $\delta E_{\perp} = 1.09\delta B_{\perp} V_{Ay}$ in $z < 0$. The ratio of $\delta E_{\perp}/\delta B_{\perp}$ has different signs in $z > 0$ and $z < 0$ due to the

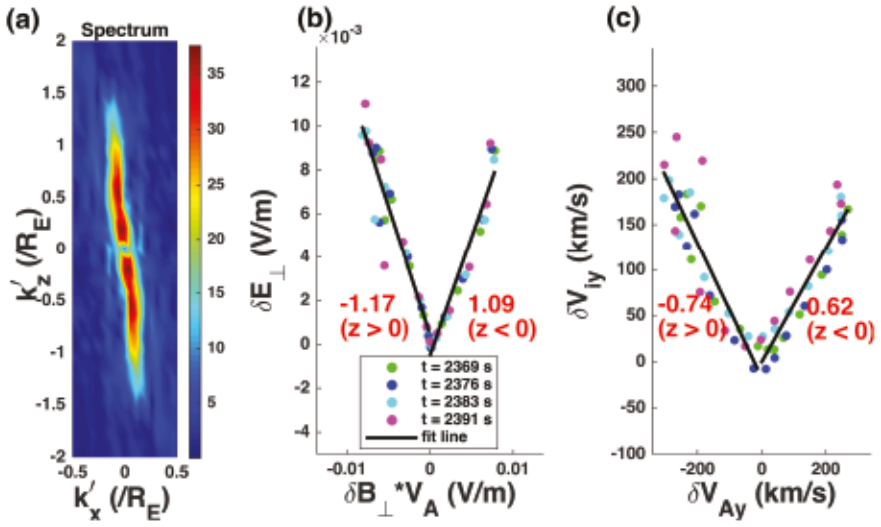

Figure 6. (a) Polarization relation and (b) Walén relation: The corresponding $\delta E_\perp$ vs $\delta B_\perp$ and δV_{Iy} vs δV_{Ay} both from $t = 2369$s to $t = 2391$s along the blue line segment marked in the contour of B_y in the plane $y = 8.0R_E$ in Figure 4b, where $\delta V_{Ay} = \delta B_y/\sqrt{\mu_0\rho}$. The solid black lines show the fitted values based on the simulation data. (c) Spectrum of $J_\parallel$ in k_x-k_z space, from $x = -15.0R_E$ to $-10.0R_E$ and from $z = -2.0R_E$ to $2.0R_E$ at $y = 8.0R_E$ marked as the black rectangle in Figure 4b.

relative direction of $k_\parallel$. Based on equation (3), the theoretically predicted ratio between the perturbation of magnetic field and electric field is $|\delta E_\perp/\delta B_\perp| \simeq 1.07V_A - 1.44V_A$. The simulation result is consistent with the theoretical polarization relation (see equation (3)) of KAWs propagating along (opposite) to the magnetic field on the north (south) side of the plasma sheet, similar to the satellite observations (Duan et al., 2016; Stawarz et al., 2017) with a super-Alfvénic velocity. Furthermore, it is seen from Figure 6c that $\delta V_{Iy} = -0.74\delta V_{Ay}$ in $z > 0$ and $\delta V_{Iy} = 0.62\delta V_{Ay}$ in $z < 0$. Note that $\frac{T_e}{T_i} \ll 1$. Based on the Walén relation, equation (7), the theoretically predicted relation between the perturbation of velocity and magnetic field is $\delta V_{Iy} \approx 0.27 - 0.77\delta V_{Ay}$. Therefore, the fit line in Figure 6c based on the simulation data is also consistent with the theory. In a word, the polarization relation and Walén relation, together with the existence of finite $J_\parallel$ and$E_\parallel$ (Figure 4), are consistent with KAWs with $k_\parallel \ll k_\perp$ and $k_\perp\rho_i \sim 1$.

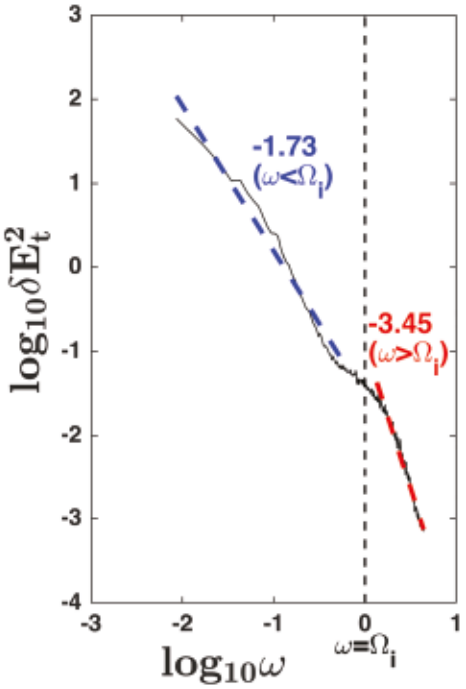

Figure 7. Spectrum of transverse electric energy density from $t = 2{,}362$ s to $t = 3{,}094$ s. The blue dash line and red dash line are the fit power laws in inertial range ($f^{-5/3}$) and dissipation range ($f^{-10/3}$), respectively.

Figure 7 shows transverse electric field power spectral density $\delta E_\perp^2(\omega)$, where $\delta E_\perp^2(\omega) = \frac{1}{TL_xL_y}\int\int \delta E_\perp^2(\omega, k_x, k_y)dk_xdk_y$ with $\delta E_\perp(\omega, k_x, k_y)$ being the 3-D FFT of $\delta E_\perp(x, y, t)$, from $x = -40.0\ R_E$ to $-10.0\ R_E$ and from $y = -10.0\ R_E$ to $10.0\ R_E$ at $z = 0.45\ R_E$ from $t = 2{,}362$ s to $t = 3{,}094$ s, where T is the time interval L_x and L_y are the length in x and y direction, respectively. A spectral break in the vicinity of $\omega \sim \Omega_i$ indicates the onset of dissipation, the energy sink at cross-scale coupling in the turbulence spectrum. At the dissipation region ($\omega > \Omega_i$), magnetic energy is coupled to thermal motions of ions. Such a turbulent spectrum is consistent with various satellite observations (Chaston et al., 2008; Leamon et al., 1998).

Virtual satellite observations of various parameters at a fixed position $(x, y, z) = (-15, 8, 0.6)R_E$ above the equator are shown in Figure 8. The gray patch marks the time interval when a KAW structure passes from $t = 2{,}290$ s to 2,505 s. Before $t = 2{,}290$ s, the value of magnetic field (B) and ion number density (N) are about 15 nT and 2.0 cm^3 in Figure 8a, denoting the virtual satellite is in the plasma sheet. From $t = 2{,}290$ to 2,505 s, the magnetic field increases, and ion density decreases, indicating this position is located in the PSBL between the plasma sheet and the northern tail lobe. After $t = 2{,}505$ s, the satellite is located in the lobe with a very low ion number density and a very high Alfvén speed V_A. In the PSBL from

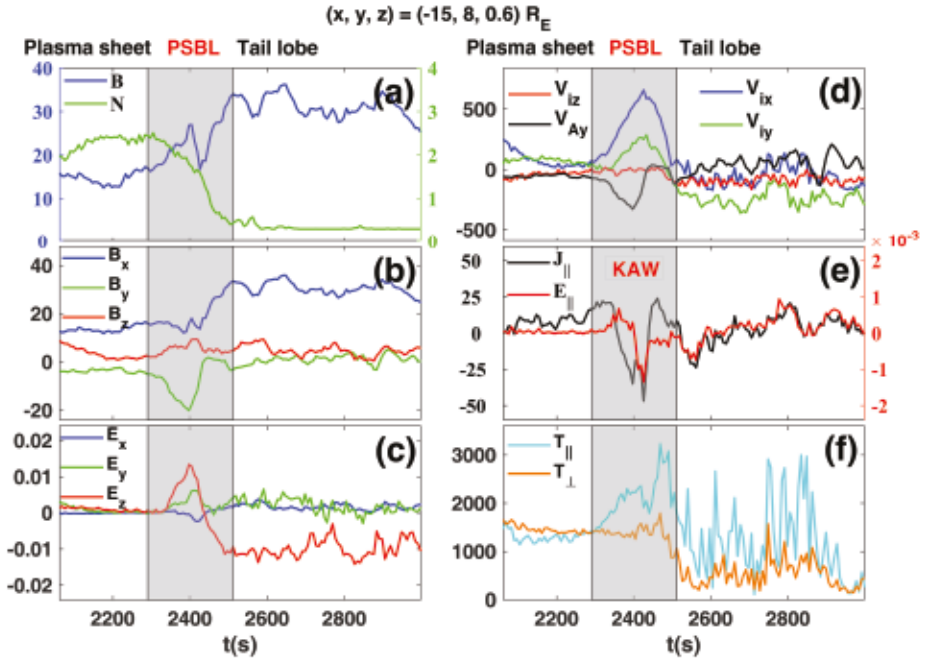

Figure 8. Time variation of (a) magnetic field and ion density; (b) x, y, and z components of magnetic filed; (c) x, y, and z components of electric filed; (d) ion flow velocity; (e) field-aligned electric field and current density; (f) parallel and perpendicular temperature from $t = 2{,}061$ s to $t = 3{,}000$ s at the position $(x, y, z) = (-15, 8, 0.6)R_E$. The gray patch marks the time interval when a KAW passes from $t = 2{,}290$ s to $t = 2{,}512$ s.

$t = 2{,}290$ to 2,505 s, the magnetic field perturbation is in B_x and B_y in Figure 8b, while the electric field perturbation is predominantly in E_z in Figure 8c. The perturbation of ion flow velocity (V_{Iy} and V_{Ix}) in Figure 8d is in the same order and negative sign with δV_{Ay}, satisfying the Walén relation of field-aligned-propagating KAWs. Meantime, field-aligned electric field ($E_\parallel$) and current density ($J_\parallel$) are well correlated in Figure 8e. All these features show that KAWs pass by this position in the plasma sheet boundary layer from $t = 2{,}290$ to 2,505 s in the PSBL. KAWs have been observed by Stawarz et al. (2017) based on an MMS event at 9 R_E in the plasma sheet, which may be associated with the BBF braking region and/or the magnetic reconnection separatrix. Similar to the MMS observation, the perturbation in magnetic field is a few tens of nT, and that in the flow speed is a few hundreds of km/s in our simulation results shown in Figure 8. The perturbation of electric field in our simulation is around 10 mV/m, which is one order smaller than that in the observation event, in which the local Alfvén speed is about one order larger than that in our simulation. Note that $E_\parallel/E_\perp$ in our simulation is larger than that predicted by linear theory (Liang et al., 2016). There is an obvious increase of parallel ion temperature and relatively smaller increase of perpendicular ion temperature in Figure 8f. Note that the increase of ion temperature may not all come from ion heating. The temperature anisotropy with $T_\parallel > T_\perp$ is consistent with the result described by Liang et al. (2017). Liang et al. (2017) presented the parallel and perpendicular heating of the accelerated ions beam by KAWs occurred simultaneously with $T_\perp > T_\parallel$ in the earlier stage, while the overall temperature anisotropy with $T_\parallel > T_\perp$ develop in the later stage due to the increase of the fraction of the accelerated ions and the interaction between the accelerated beam and the core population.

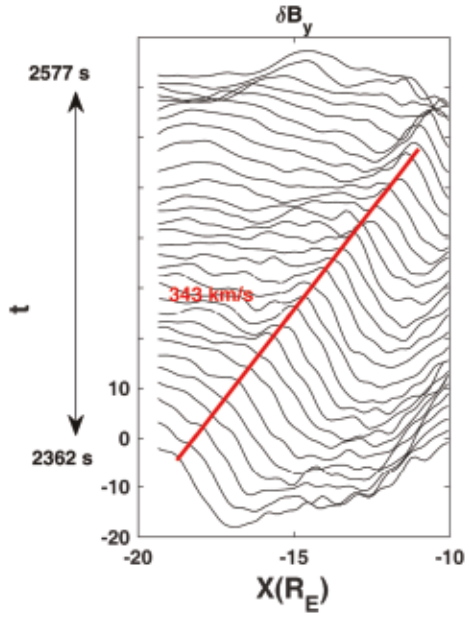

Figure 9. The time sequence of the spatial cuts of of δB_y from $t = 2{,}362$ s to $t = 2{,}577$ s along $z = 0.75R_E$ at $y = 7.5R_E$ from $x = -19R_E$ to $-10R_E$.

Figure 9 shows the time sequence of δB_y as a function of x from $t = 2{,}362$ s to $t = 2{,}577$ s along $z = 0.75R_E$ at $y = 7.5R_E$. The wave propagation speed of the KAWs can be measured by tracking the propagation of the wavefront as indicated by the red line. The phase speed of KAWs is nearly along

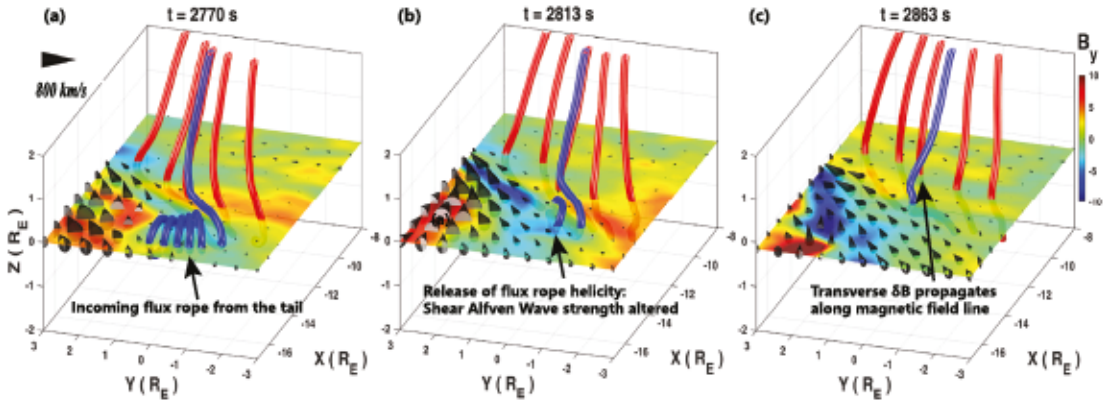

Figure 10. Contours of B_y at (a) $t = 2{,}770$ s, (b) $t = 2{,}813$ s in the plane $z = 0R_E$, and (c) $t = 2{,}863$ s in the plane $z = -0.3R_E$ (the center of plasma sheet is not always in the equatorial plane) with typical magnetic field lines.

the magnetic field, which is nearly along the x direction, and their group velocity is along the magnetic field. The phase speed is estimated from the slope of the red line as 343 km/s in the simulation frame. Note that the background convection speed is very small and can be ignored and the ion flow is nearly perpendicular to the background magnetic field. Thus, the phase speed of the wave is larger than the local Alfvén speed of ~290 km/s, consistent with the feature of KAWs with $k_\perp \rho_i \sim 0.6$.

3.3. KAWs in the Flow-Braking Region and Penetration of Poynting Flux

As the shear Alfvén waves generated in the tail plasma sheet encounter the strong dipole-like field in the flow-braking region, their wave power is found to be altered. Take flux ropes (also carrying shear Alfvénic magnetic field perturbations) as an example. At $t = 2{,}770$ s, the flux rope from the magnetotail as shown in blue in Figure 10a arrives at $x = -15R_E$, carried by a fast flow. Due to the flow braking, sheared flow is present in the azimuthal direction, as marked as black cones (see Figure 10a.) which causes perturbations in the dawn-dusk component of the magnetic field. While shear flow alone can generate shear Alfvén waves (Dobrowolny, 1972, 1977; Wang et al., 1998), in our case the flow shear is found to alter the incoming flux rope helicity at the flow shear interface. At the dipole-like field region around the equator at $t = 2{,}813$ s, the flux rope around $x = -12R_E$ releases its helicity (see Figure 10b). This process alters the strength of shear Alfvén waves, which can be distinguished by the change of B_y structure. Finally, the helicity of the flux rope is fully released at $t = 2{,}863$ s, and the perturbation of transverse magnetic field propagates away from the equatorial plane along magnetic field lines (see Figure 10c.).

In addition, ion inertial effects are found to lead to the generation of additional KAWs at the boundary between the tail-like and dipole-like field, as illustrated in Figure 11. Besides the KAW structure highlighted by black rectangles (shown for the midnight-meridian plane and the plane $z = 0.5 \quad R_E$) in Figure 11a propagating from the magnetotail, new KAWs marked as white rectangles in Figure 11a are generated at the inner edge of the flow-braking region in front of the dipole-like field. This is due to ion inertial effects. Figures 11b and 11c shows the generation and propagation of the new KAWs in the midnight-meridian plane and the plane $z = 0.5R_E$, respectively. The black arrows in these figures show the flow vectors. At $t = 2{,}870$ s, there is no signature of KAWs in the near-Earth region of $x > -11R_E$, and a close examination of the flow vectors shows that fast flows have also not arrived there yet. This is because magnetotail reconnection is firstly initiated on the dawnside and duskside close to the equatorial magnetopause, not in the midnight region. It is developed in the midnight region at a later time. Nevertheless, at $t = 2{,}920$ s in Figures 11b and 11c, fast flows due to reconnection have arrived at $x \simeq -11R_E$ in this midnight region, and there are well-correlated structures in B_y, $J_\parallel$, and $E_\parallel$ (marked as the white circles), exhibiting the features of KAWs similar to Figure 4. In this region, charge separation occurs because of the larger inertia of ions than electrons. Ions penetrate deeper into the magnetosphere before being stopped by the strong magnetic field. As a result, a pair of parallel currents appear, as previously found by Swift and Lin (2001) based on a 2-D global hybrid simulation. The wave power increases at $t = 2{,}963$ s. Then, the waves propagate to the high latitudes along magnetic field lines. At $t = 3{,}035$ s, the waves have gone further away from the equatorial plane and cannot be shown in the plane of $z = 0.5R_E$. A global diploarization is also seen over the time period from $t = 2{,}870$ s to $t = 3{,}035$ s,

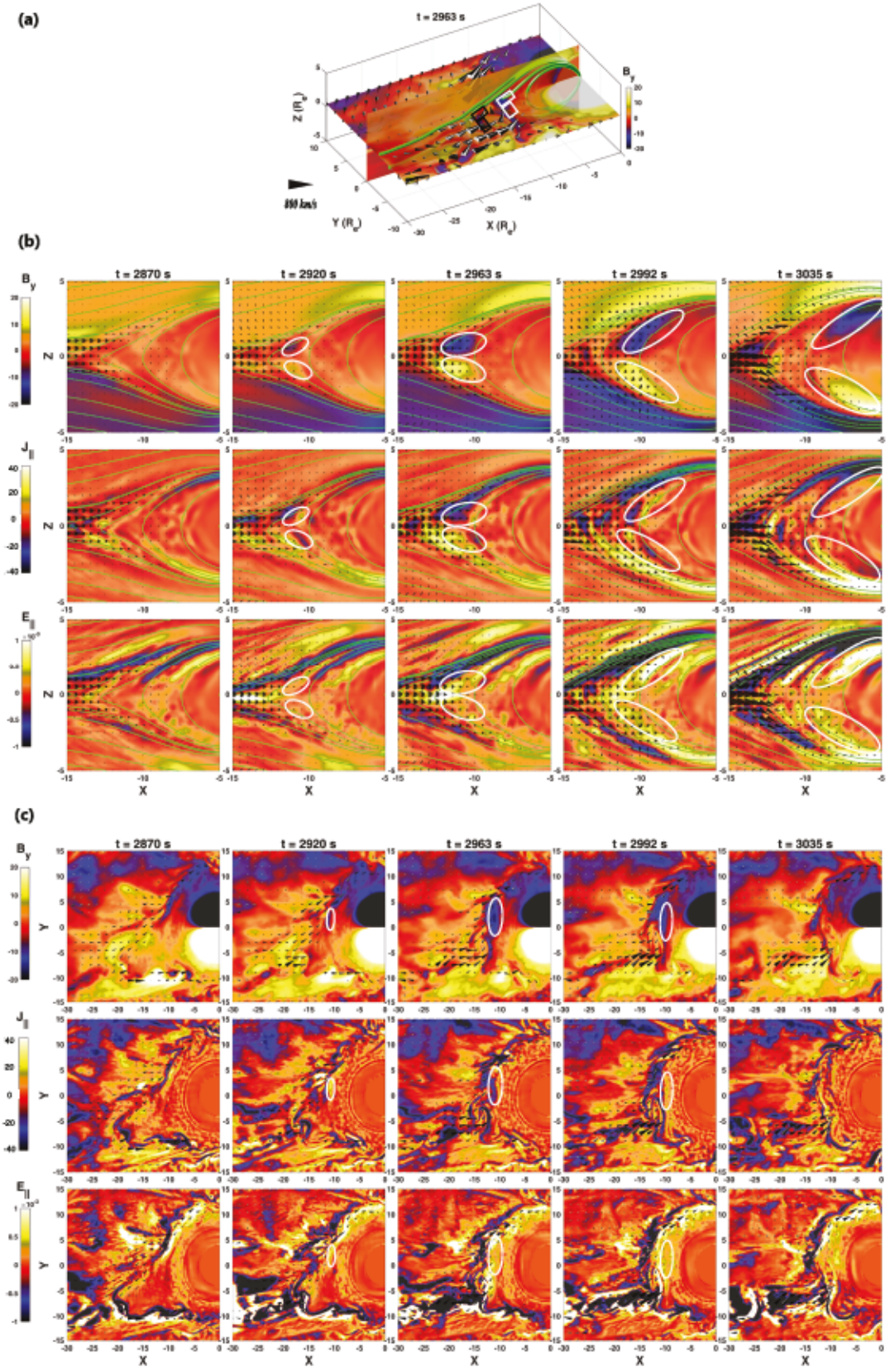

Figure 11. (a) Contours of B_y in the equatorial and noon-meridian plane at $t = 2{,}963$ s; time variation of contours of transverse magnetic filed (B_y) and parallel current density ($J_\parallel$), parallel electric field ($E_\parallel$) in the plane (b) $y = 0R_E$ and (c) $z = 0.5R_E$ in a time sequence of $t = 2{,}870$ s, $t = 2{,}920$ s, $t = 2{,}963$ s, and $t = 3{,}035$ s.

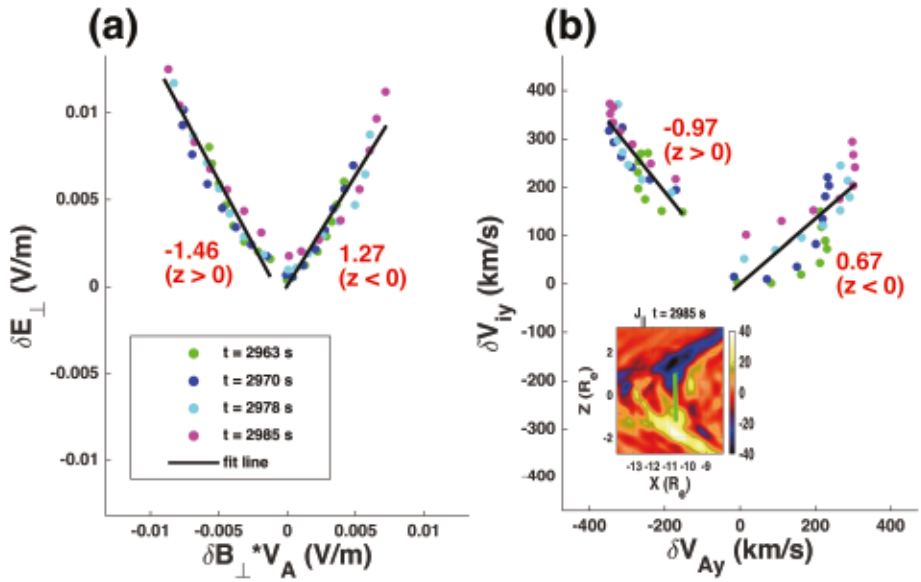

Figure 12. (a) Polarization relation and (b) Walén relation: the corresponding $\delta E_\perp$ versus $\delta B_\perp$ and δV_{iy} versus δV_{Ay} both from $t = 2{,}963$ s to $t = 2{,}985$ s along the green line segment marked in the contour of $J_\parallel$ in Figure 12b in the plane $y = 0 \quad R_E$. The solid black lines show the fitted values based on the simulation data.

which causes the expansion of the dipole-like geomagnetic field region. Figure 11c shows the corresponding structures in the plane $z = 0.5R_E$. The localized structures highlighted by the white circles in Figure 11c are the near-equatorial counterparts of these new KAWs. These waves are identified as KAWs in the same manner as the waves in the magnetotail (see Figure 6).

Figure 12 shows the polarization relation and Walén relation along the green line marked in the contour plot of $J_\parallel$ in Figure 12b. $\delta E_\perp$ and $\delta B_\perp$ in Figure 12a are also well correlated, with $\delta E_\perp = -1.46\delta B_\perp V_{Ay}$ in $z > 0$ and $\delta E_\perp = 1.27\delta B_\perp V_{Ay}$ in $z < 0$. The ratio of $\delta E_\perp/\delta B_\perp$ in $z > 0$ and $z < 0$ has different signs due to the opposite direction of $k_\parallel$. The perpendicular wave number $k_\perp \rho_i \sim 0.2-1.1$ in these waves. The polarization relation in Figure 12a is consistent with the theoretically predicted ratio with $|\delta E_\perp/\delta B_\perp| \simeq 1.02V_A - 1.48V_A$ based on equation (3). Based on equation (7), the theoretically predicted relation between the perturbation of velocity and magnetic field is $\delta V_{iy} \approx 0.27 - 0.93\delta V_{Ay}$. The Walén relation in Figure 12b with $\delta V_{iy} = -0.97\delta V_{Ay}$ in $z > 0$ and $\delta V_{iy} = 0.67\delta V_{Ay}$ in $z < 0$ is also consistent with theory.

Figure 13 presents the time variations of the same quantities as shown in Figure 8 at $(x, y, z) = (-11.1, 0.5, 0.6)R_E$ in the flow-braking region. Before $t = 2{,}870$ s, B_x is dominant, $B_z \ll B_x$, and thus, the magnetic field line is more stretched (see Figure 13b). The flow velocity is very small, as seen from Figure 13d, indicating there is no fast flow yet at this near-midnight location. The shaded region from $t = 2{,}870$ s to $t = 3{,}034$ s shows one event of KAWs generated around this position. A pulse of B_y is generated during this time interval, as shown in Figure 13b. Near the end of the interval, the background B_x decreases while B_z, the field strength B (as shown in Figure 13a), and the average ion perpendicular temperature (as shown in Figure 13f) also have a sharp increase, indicating that the position is now inside the dipole-like region due to the global dipolarization and the B_y wave pulse is located just at the edge of the dipole-like field region. Unlike the KAWs in the magnetotail, here near the flow braking, V_{ix} from $t = 2{,}870$ s to $t = 3{,}034$ s is very small (see Figure 13d). While the perturbation of the magnetic field is mainly in the y direction, the pulse of electric field perturbation has both E_x and E_z components (see Figure 13c) since $k_\perp$ is oblique in the xz plane. Correspondingly, the wave pulse is also seen in V_{iy} and V_{Ay} (Figure 13d), $J_\parallel$ and $E_\parallel$ (Figure 13e), and both ion temperatures $T_\parallel$ and $T_\perp$ (Figure 13f). Note that compressional wave perturbations are also frequently present in the flow-braking region. As seen in Figure 13, just a few tens of seconds after $t = 3{,}037$ s, a large-amplitude compressional wave pulse is generated, with clear enhancements in B and ion perpendicular temperature. There is an antiphase correlation between B and N.

Since shear Alfvén waves/KAWs generated in the equatorial magnetotail must interact with the transition region between the tail-like and dipole-like fields before they can propagate to the ionosphere, as discussed

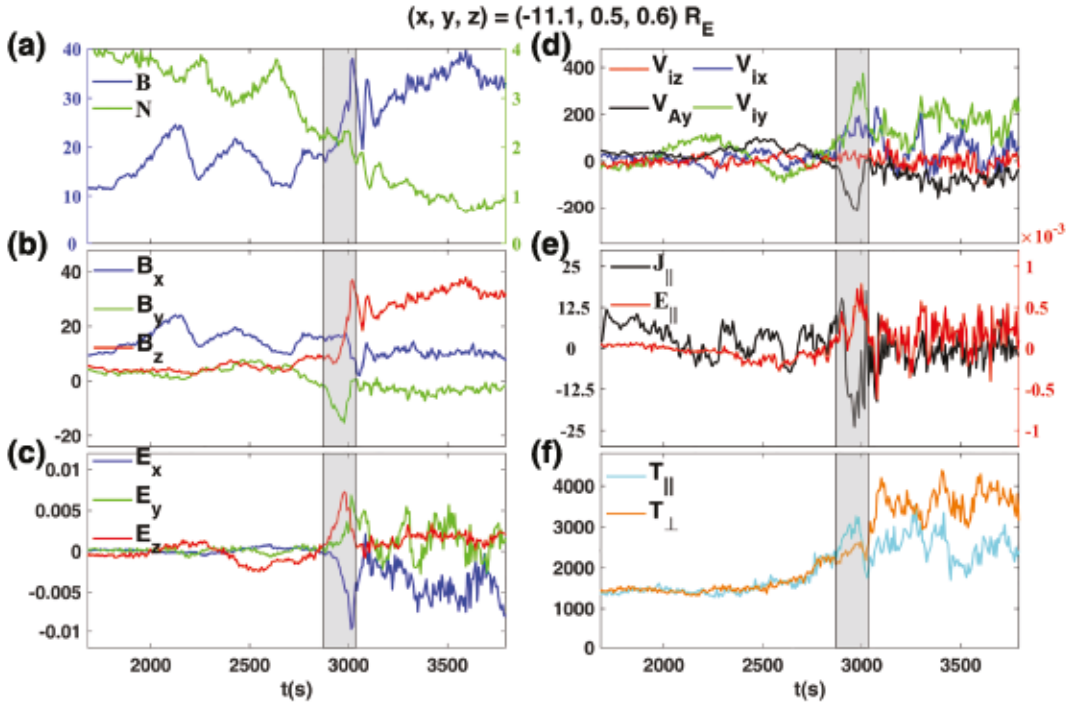

Figure 13. Time variation of (a) magnetic field and ion density; (b) x, y, and z components of magnetic filed; (c) x, y, and z components of electric filed; (d) ion flow velocity; (e) field-aligned electric field and current density; and (f) parallel and perpendicular temperature from $t = 1{,}682$ s to $t = 3{,}794$ s at the position $(x, y, z) = (-11.1, 0.5, 0.6)$ R_E. The shaded region from $t = 2{,}870$ s to $t = 3{,}034$ s shows one event of KAWs generated around this position.

above, it is important to understand whether the Poynting flux follows a direct mapping from the plasma sheet to the ionosphere. In the following we estimate how much Alfvénic wave energy can be transmitted across this transition region around $r \sim 10.0$ R_E. Figure 14a shows the contours of B in the equatorial plane at $t = 2{,}548$ s, with ion flow velocity superposed as black arrows. Colored lines in the figure are a magnetic flux tube tracked from $t = 2{,}491$ s to $t = 2{,}548$ s. The transition region between the dipole-like magnetic field region and the tail-like region is around $r = 10.0$–11.0 R_E. Note that the dashed lines in the equatorial plane in Figure 14a mark various geocentric distances. The ratio between the parallel Poynting flux and the magnetic field strength, $S_\parallel/B$, along the field line as a function of the latitude α at various times is shown in Figure 14b, where $\alpha = 90° - \theta$ with θ being the polar angle. At $t = 2{,}491$ s, the flux tube is stretched tail-like around the equator, going through the plasma sheet. As time proceeds, the flux tube moves earthward. If there were steady driving of Alfven waves and all the wave power in the plasma sheet propagated into the inner magnetosphere along the flux tube, the ratio $S_\parallel/B$ should tend to be nearly a constant, considering that the flux tube cross section area is inversely proportional to B. The results in Figure 14b, however, show clearly that not all the wave energy reaches the ionosphere. Overall, the value of $S_\parallel/B$ is quite different between the tail-like part of the field line (near equator, with $\alpha < 10°$) and dipole-like region (higher latitudes). The ratio remains nearly constant only inside the dipole-like field region ($\alpha > 30°$) on the earthward side of the tail-dipole transition region, as seen from Figure 14b.

At $t = 2{,}491$ s, $S_\parallel/B$ peaks at $\alpha \simeq 3°$ near the equator where the source of KAW in the tail is, which is outside the transition region, with the peak value $\sim 10.5 \times 10^{-6}$ W/(m^{2}nT). As discussed in Figure 10, the structure of KAWs from the tail are then significantly altered by the flow-braking region. A dip is seen in the ratio $S_\parallel/B$ at $\alpha \simeq 7°$, and then another much weaker peak appears, associated with the Poynting flux both transmitted from the magnetotail and locally generalized, which only reaches 1.7×10^{-6} W/(m^{2}nT) at $\alpha = 13°$ in Figure 14b for $t = 2{,}491$ s. The ratio then decreases from $\alpha = 13°$ to $\alpha = 30°$, which is likely due to ion Laudau damping. The ratio then reaches nearly constant in $\alpha > 30°$.

At $t = 2{,}513$ s, the peak value of $S_\parallel/B$ near the equator has decreased to about 6.2×10^{-6} W/(m^{2}nT) as the tail flux tube moves closer to the Earth and some waves have propagated away from the equator. Again, $S_\parallel/B$ decreases significantly from the tail-like to dipole-like field region. The tail KAWs continue to propagate

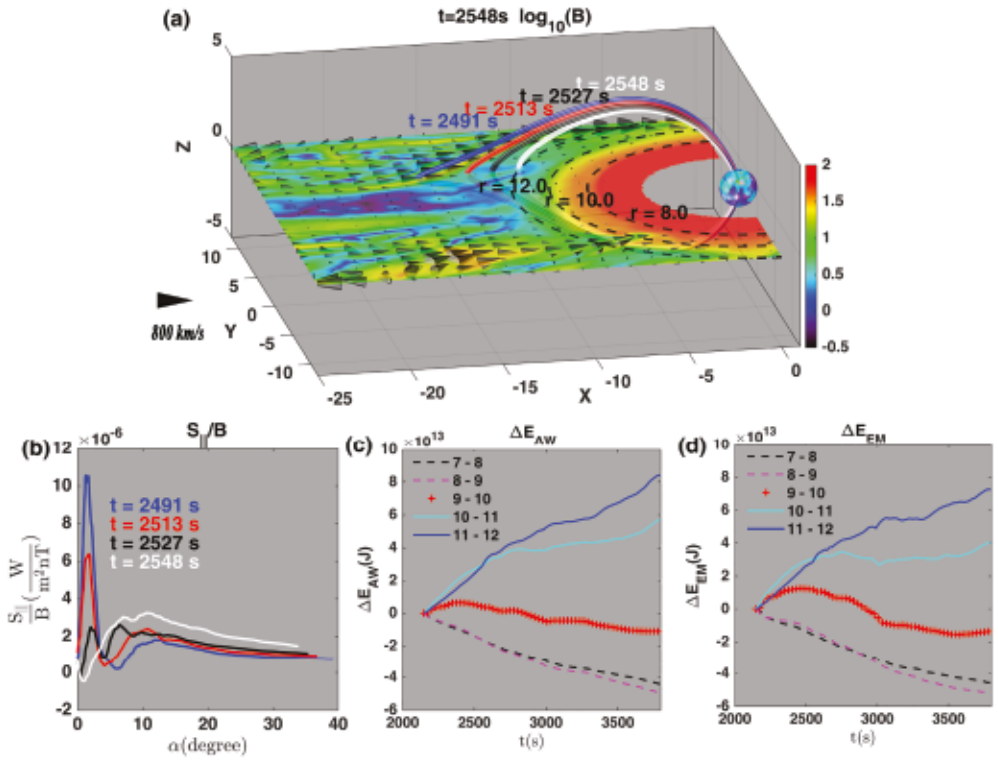

Figure 14. (a) Contour of B in the equatorial plane at $t = 2{,}548$ s; (b) line plots of $S_{||}/B$ versus α along a tracked magnetic flux tube as shown in Figure 14a at $t = 2{,}491$ s (blue), $t = 2{,}513$ s (red), $t = 2{,}527$ s (black), and $t = 2{,}548$ s (white), respectively, where $\alpha = 90° - \theta$ with θ being the polar angle; time evolution of (c) Alfvénic wave energy (ΔE_{AW}) and (d) electromagnetic wave energy (ΔE_{EM}) flowing out of the spherical shell over the nightside from $t = 2{,}147$ s to $t = 3{,}794$ s with black dash line from $r = 7.0 \quad R_E$ to $r = 8.0 \quad R_E$, magneta dash line from $r = 8.0R_E$ to $r = 9.0R_E$, red line from $r = 9.0R_E$ to $r = 10.0R_E$, cyan line from $r = 10.0R_E$ to $r = 11.0R_E$, and blue line from $r = 11.0R_E$ to $r = 12.0R_E$. Parts of the interface between the surface of the sphere and the equatorial plane are marked as black dash curves in Figure 14a.

away at $t = 2{,}527$ s. By $t = 2{,}548$ s, the flux tube has moved to $L \simeq 12 \quad R_E$ (see the white field line in Figure 14a), and the wave energy has spread out over the field line. At later times, part of Shear Alfvén wave/KAW energy is seen to be reflected at the inner boundary, similar to that described in Guo et al. (2015). Given that the average Alfvén speed along a tracked magnetic flux tube is around 1,500 km/s, it takes about 80–100 s for Shear Alfvén waves/KAWs to arrive at the inner boundary and be reflected. The peak values of $S_{||}/B$ at $\alpha \simeq 3°$ at $t = 2{,}491$ s and $t = 2{,}548$ s are roughly corresponding to the initial and final stage, respectively, of the source Poynting flux associated with a fast flow event outside the transition region. The difference between these two peak values is $\sim 10.5 \times 10^{-6} \quad \mathrm{W/(m^2 nT)}$ as the source Alfvénic energy from the tail propagates away over this time interval. Similarly, the difference between the two peak values at $\alpha \simeq 13°$, $\sim 1.5 \times 10^{-6} \quad \mathrm{W/(m^2 nT)}$, roughly corresponds to the increase of Alfvénic energy in the dipole-like field region as a result of the fast flow event. Such a result indicates that a factor of less than $1.5 \times 10^{-6}/10.5 \times 10^{-6} \sim 1/7$ of the Alfvénic wave energy from the magnetotail goes across the transition region into the dipole-like field region during the fast flow period. After a decreasing of the wave power over α, the values of $S_{||}/B$ remain nearly constant in α for $\alpha > 30°$ with $S_{||}/B \sim 1.49 \times 10^{-6} \quad \mathrm{W/(m^2 nT)}$ at $t = 2{,}491$ s and $S_{||}/B \sim 0.77 \times 10^{-6}$ W/(m^{2}nT) at $t = 2{,}548$ s. As a result, the Poynting flux received in the ionosphere during the period from $t = 2{,}491$ s to $t = 2{,}548$ s can be estimated as $\sim 0.72 \times 10^{-6} \quad \mathrm{W/(m^2 nT)}$. Overall, roughly less than $0.72 \times 10^{-6}/10.5 \times 10^{-6} \sim 1/14$ of the Alfvénic wave energy from the magnetotail fast flow reaches the ionosphere.

Figure 14c shows the time evolution of Alfvénic wave energy (ΔE_{AW}) flowing out of the spherical shell over the nightside for different radii, where $\Delta E_{AW}(r_1, r_2, t) = E_{AW}(r_1, t) - E_{AW}(r_2, t)$ with $E_{AW}(r, t)$ being written as

$$E_{\mathrm{AW}}(r,t) = -\int_{t'=2147}^{t'=t}\int_{\phi=\pi/2}^{\phi=3\pi/2}\int_{\theta=0}^{\theta=\pi} \mathbf{S}_{\parallel}\cdot\hat{\mathbf{r}}\mathbf{r}^2\sin(\theta)\,\mathrm{d}\theta\,\mathrm{d}\phi\,\mathrm{d}t', \tag{13}$$

with $\hat{\mathbf{r}}$ being the unit vector in the radial direction and (r, θ, ϕ) giving the radial distance, polar angle, and azimuthal angle. From $r = 12.0R_E$ to $r = 10.0R_E$, the total Alfvénic wave energy is increasing as seen by an over all increasing positive ΔE_{AW} (see the blue and cyan line), which means there are new sources of shear Alfvén wave coming from the tail to the tail-dipole field transition region.

In the dipole-like field region, the wave energy decreases from $r = 9.0R_E$ to $r = 7.0R_E$ as seen by an overall decreasing negative ΔE_{AW}(see the black and magenta line) in Figure 14c. Evidence of the decrease of shear Alfvénic wave energy from the magnetotail to the inner magnetosphere can also be seen in Figure 14b. Such a decrease may be due to ion Landau damping. Note that our simulation also shows that shear Alfvén waves/KAWs are present throughout the inner magnetosphere (Lin et al., 2014). The presence of KAWs, including kinetic field-line resonance, in the inner magnetosphere has been observed by Chaston et al. (2014). They may be generated by mode conversion from compressional waves that propagate across the field lines from the tail. Such a process of coupling between the compressional and transverse modes and the excitation of resonant waves (Lysak et al., 2015) will be investigated elsewhere.

The total Alfvénic wave energy varies in time and would not be keeping decreasing or increasing in the region from $r = 10.0R_E$ to $r = 9.0R_E$ (see the red line in Figure 14c.). That is because this region is not always in the tail-dipole field transition region or dipole-like field region. For example, the region is located in the tail-dipole field transition region, and ΔE_{AW} is increasing from $t = =2{,}147$ s to $t = 2{,}404$ s. From $t = 2{,}404$ s to $t = 2{,}662$ s, the region is located in the dipole-like field region due to the global dipolarization, and ΔE_{AW} is decreasing.

To assess the contribution of the new local source and external source to E_{AW}, Figure 14d shows the time evolution of electromagnetic wave energy, (ΔE_{EM}), flowing out of the spherical shell over the nightside for different radii. The quantity E_{EM} is calculated in a similar way as E_{AW} by substituting $\mathbf{S}_{\parallel}$ with $\mathbf{S}$. The increase of ΔE_{AW} seen in the transition region in Figure 14c by itself does not establish that there is local generation of the Alfvén waves because parallel Poynting flux could arise through a mode conversion process. However, if the development of parallel Poynting flux were the result of mode conversion, it would not change E_{EM}. Overall, the lines in Figure 14d have the same trends with those in Figure 14c. However, $\Delta E_{EM}(11, 12, t)$ and $\Delta E_{EM}(10, 11, t)$ at $t = 3{,}794$ s have a value of 7.3×10^{13} J and 4.1×10^{13} J, respectively, smaller than $\Delta E_{AW}(11, 12, t)$ and $\Delta E_{AW}(10, 11, t)$ with a value of 8.5×10^{13} J and 5.7×10^{13} J, respectively. This is because parts of compressional wave energy are converted to Alfvénic wave energy. In a word, the generation of much of the wave energy is local while some of the wave generation is likely due to mode conversion.

4. Conclusions and Discussion

In this paper, the generation and propagation of KAWs in the magnetotail are studied via a 3-D global hybrid simulation based on Auburn Global Hybrid Code in 3-D. The main results are as follows:

1. KAWs are generated by the near-tail reconnection, propagating earthward and tailward. As part of the structure of the reconnection, the electromagnetic fluctuations, parallel electric, parallel currents, and parallel Poynting fluxes are carried by KAWs to the ionosphere. These highly 3-D Alfvénic waves with $k_{\perp} \gg k_{\parallel}$ are identified by the polarization and dispersion relations of Alfvén modes. The spectral break of the electromagnetic power spectral density shows that ion kinetic physics begin to show up at $\omega \sim \Omega_i$.
2. As the shear Alfvén waves generated in the tail plasma sheet encounter the strong dipole-like field in the flow braking region, their wave power is found to be altered.
3. KAWs are also generated at the inner edge of flow-braking region in front of the dipole-like field due to the ion inertial effects. Polarization and dispersion relations of these waves are also presented in this paper.
4. The total Alfvénic wave energy on the nightside is estimated. Roughly less than 1/7 of Alfvénic wave energy originating from magnetotail reconnection can cross the transition region around $r = 10.0\,R_E \sim 11.0\,R_E$, and less than 1/14 of the Alfvénic wave energy from the magnetotail reaches the ionosphere. Magnetotail reconnection, local sources at the flow-braking region, and mode conversion are the sources of Alfvénic wave energy of the ionosphere.

It should be pointed out that as the wave propagates closer to the ionosphere, they will be in the inertial regime when β is less than the electron-to-ion mass ratio m_e/m_i. Nevertheless, inertial Alfvén waves are not included in the hybrid model, in which electrons are considered as a massless fluid. Electron Landau damping is also ignored in the model.

The parallel electric field is clearly present in the polarization of KAWs, but its magnitude in our simulation appears to be larger than that predicted by the linear theory. The magnetic field perturbations in the KAWs generated in the tail fast flows are of large amplitude (e.g., Figure 8), and the waves are localized, embedded in the nonuniform plasma. This introduces uncertainty in the estimate of $E_\parallel$. In our diagnostics, we have calculated $E_\parallel$ by projecting **E** to the wavy local magnetic field **B**.

Overall, our simulation presents a comprehensive picture of the generation and structure of KAWs in the global magnetosphere as well as their connection to the ionosphere. The shear Alfvén waves and KAWs are shown to be significant carriers of the parallel currents and Poynting fluxes that are injected to the ionosphere. Nevertheless, due to the presence of multiple boundary/transition layers in the magnetosphere, the magnitude of Poynting fluxes in the tail KAWs is not simply mapped to the ionosphere.

Appendix A: Derivation of Walén Relation for KAWs

The set of the basic equations based on the kinetic-fluid theory (Cheng & Johnson, 1999) can be written as

$$\rho\frac{d\mathbf{V}}{dt} = \mathbf{J}\times\mathbf{B} - \nabla\cdot\mathcal{P} - \nabla\cdot\Pi, \tag{A1}$$

$$\frac{d\rho}{dt} = -\rho\nabla\cdot\mathbf{V}, \tag{A2}$$

$$\frac{\partial\mathbf{B}}{\partial t} = -\nabla\times\mathbf{E}, \tag{A3}$$

$$\nabla\times\mathbf{B} = \mathbf{J}, \tag{A4}$$

where ρ and $\mathbf{V}$ are mass density and bulk velocity of one fluid, respectively, and $\mathcal{P}$ and Π are diagonal pressure tensor element and off-diagonal pressure tensor element, respectively. The charge quasi-neutrality condition, $n_e e = \sum_i n_i q_i$, is assumed. Substituting the $\mathbf{J}\times\mathbf{B}$ term in equation (A1) using the perpendicular generalized Ohm's law (Krall & Trivelpiece, 1973) and ignoring electron inertial terms, we have

$$\mathbf{E}_\perp + \mathbf{V}\times\mathbf{B} = \frac{1}{n_e e}\nabla_\perp\cdot(\mathcal{P}+\Pi) + \rho\frac{d\mathbf{V}_\perp}{dt}. \tag{A5}$$

The gyroviscosity contribution is given by Cheng and Johnson (1999)

$$\nabla_\perp\cdot\Pi = \nabla_\perp\delta P_c + \hat{\mathbf{b}}\times\nabla_\perp\delta P_s, \tag{A6}$$

where $\hat{\mathbf{b}}$ is the unit vector along the background magnetic field, $\delta P_c = \int d^3v\frac{mv_\perp^2}{2}\cos 2\theta\delta f$, and $\delta P_s = \int d^3v\frac{mv_\perp^2}{2}\sin 2\theta\delta f$ with θ being the particle gyrophase angle between $\hat{\mathbf{b}}$ and $\hat{\mathbf{k}}_\perp$(the unit vector along the perpendicular wave vector directions). Fourier transforming fields and ignoring the background gradients and parallel magnetic field fluctuations (this approximation is valid for the whole derivation), the following equation can be obtained from equation (A5):

$$\mathbf{V}_\perp\times\mathbf{B} + \left(\Gamma_0 - \Gamma_1\right)\mathbf{E}_\perp = 0, \tag{A7}$$

where $\Gamma_n = I_n(b)e^{-b}$, with $b = k_\perp^2\rho_i^2$ and I_n being the modified Bessel function of first kind of order n. The gyroviscosity term is conveniently considered together with the $\rho\frac{d\mathbf{V}_\perp}{dt}$ term because

$$\hat{\mathbf{b}}\times\nabla_\perp\delta P_s = \left(\frac{1-\Gamma_0}{b} - \left(\Gamma_0-\Gamma_1\right)\right)\rho\frac{\partial}{\partial t}\frac{\mathbf{E}\times\mathbf{B}}{B^2}. \tag{A8}$$

Let us define a new velocity variable

$$\tilde{\mathbf{V}} \equiv \mathbf{V} + \left(\frac{1-\Gamma_0}{b} - \left(\Gamma_0-\Gamma_1\right)\right)\frac{\mathbf{E}\times\mathbf{B}}{B^2}. \tag{A9}$$

The Ohm's law is then reduced to

$$\tilde{\mathbf{V}} = \frac{1-\Gamma_0}{b}\frac{\mathbf{E}\times\mathbf{B}}{B^2}, \tag{A10}$$

where

$$\tilde{\mathbf{V}} = \frac{1-\Gamma_0}{b}\frac{1}{\Gamma_0-\Gamma_1}\mathbf{V}. \tag{A11}$$

In transforming these equations to real space from their Fourier representation, we employ the Padé approximation, which leads to

$$\frac{1-\Gamma_0}{b} \sim \frac{1}{1+b} \tag{A12}$$

and

$$\left(\frac{1-\Gamma_0}{b}\right)\frac{1}{\Gamma_0-\Gamma_1} \sim 1+1.25b. \tag{A13}$$

The Padé approximation implies upon inversed Fourier transform that

$$\left(1-\rho_i^2\nabla_\perp^2\right)\tilde{\mathbf{V}}_\perp \approx \frac{\mathbf{E}\times\mathbf{B}}{B} \tag{A14}$$

and

$$\left(1-1.25\rho_i^2\nabla_\perp^2\right)\mathbf{V}_\perp \approx \tilde{\mathbf{V}}_\perp. \tag{A15}$$

Using equations (A14) and (A15), the momentum equation and the Faraday's law can be written as

$$\rho\frac{\partial\tilde{\mathbf{V}}}{\partial t}+\mathbf{V}\cdot\nabla\mathbf{V} = \mathbf{B}\cdot\nabla\mathbf{B}-\nabla\left(P+B^2/2\right) \tag{A16}$$

and

$$\frac{\partial\mathbf{B}}{\partial t} = \left(1-\rho_i^2\nabla_\perp^2\right)\left(\mathbf{B}\cdot\nabla\tilde{\mathbf{V}}-\mathbf{B}\nabla\cdot\tilde{\mathbf{V}}-\tilde{\mathbf{V}}\cdot\nabla\mathbf{B}\right)-\nabla\times\mathbf{E}_\parallel, \tag{A17}$$

respectively. Based on the parallel Ohm's law,

$$\frac{m_e}{n_e e^2}\partial\mathbf{J}_\parallel/\partial t = -\frac{m_e}{n_e e^2}\mathbf{b}\cdot\nabla\times(\nabla\times\mathbf{E}) = \mathbf{E}_\parallel+\frac{1}{n_e e}\nabla P_e, \tag{A18}$$

the parallel electric field can be written as

$$\left(1-\lambda_e^2\nabla_\perp^2\right)\mathbf{E}_\parallel = -\lambda_e^2\nabla_\parallel\nabla_\perp\cdot\mathbf{E}_\perp-\frac{T_e}{e\rho}\nabla_\parallel\rho, \tag{A19}$$

where λ_e is the electron skin depth. Using Ohm's law and keeping terms to order ω/Ω_i, the continuity equation can be expressed as

$$\frac{1}{\rho}\frac{d\rho}{dt} = \frac{e}{m_i\Omega_i^2}\mathbf{B}\times\nabla_\perp\cdot\partial\tilde{\mathbf{V}}/\partial t+\frac{\mathbf{B}\cdot\partial\mathbf{B}/\partial t}{B^2}. \tag{A20}$$

Neglect compressional effects and background gradients in equation (A20). Then equation (A19) can be simplified as

$$\left(1-\lambda_e^2\nabla_\perp^2\right)E_\parallel = -\left(\rho_s^2-\lambda_e^2\left(1-\rho_i^2\nabla_\perp^2\right)\right)\nabla_\parallel\left(\mathbf{B}\times\nabla_\perp\cdot\tilde{\mathbf{V}}\right), \tag{A21}$$

where $\rho_s^2 \equiv \left(T_e/T_i\right)\rho_i^2$ is the ion acoustic gyroradius.

Finally, the perpendicular terms of equations (A16) and (A17) in the homogeneous limit in the Fourier representation are written as

$$\omega\rho\delta\tilde{\mathbf{V}}_\perp = -k_\parallel B_0\delta\mathbf{B}_\perp+\mathbf{k}_\perp\left(\delta P+B_0\delta B_\parallel\right) \tag{A22}$$

and

$$\omega\delta\mathbf{B}_\perp = -k_\parallel B_0\left(1+k_\perp^2\rho_i^2\right)\delta\tilde{\mathbf{V}}_\perp-\mathbf{b}\times\mathbf{k}_\perp E_\parallel. \tag{A23}$$

Equation (A21) in the Fourier representation is written as

$$\left(1+k_\perp^2\lambda_e^2\right)E_\parallel = k_\parallel B_0\left(\rho_s^2-\lambda_e^2\left(1+k_\perp^2\rho_i^2\right)\right)\mathbf{b}\times\mathbf{k}_\perp\cdot\delta\tilde{\mathbf{V}}_\perp. \tag{A24}$$

Combining equations (A23) and (A24), we obtain the relation between the perturbed magnetic field and velocity as

$$\omega\delta\mathbf{B}_\perp = -k_\parallel B_0\frac{1+\left(1+T_e/T_i\right)k_\perp^2\rho_i^2}{1+k_\perp^2\lambda_e^2}\delta\mathbf{V}_\perp. \tag{A25}$$

The projection in the $\mathbf{b}\times\mathbf{k}_\perp$ direction of equations (A22) and (A24) gives the KAW/SAW dispersion relation:

$$\omega^2 = k_\parallel^2 V_A^2\frac{1+\left(1+T_e/T_i\right)k_\perp^2\rho_i^2}{1+k_\perp^2\lambda_e^2}. \tag{A26}$$

Combing equations (A11), (A13), (A25), and (A26) and considering $\delta\mathbf{V}\approx\delta\mathbf{V}_i$, the Walén relation for KAWs is given by

$$\delta\mathbf{V}_i \approx \pm\delta\mathbf{V}_A\left(\frac{1+k_\perp^2\lambda_e^2}{1+\left(1+\frac{T_e}{T_i}\right)k_\perp^2\rho_i^2}\right)^{1/2}\left(\frac{1}{1+1.25k_\perp^2\rho_i^2}\right), \tag{A27}$$

where the coefficient $\frac{1}{1+1.25k_\perp^2\rho_i^2}$ comes from the gyroviscosity in the pressure tensor.

Acknowledgments
This work was supported by NASA (NNX17AI47G) and National Science Foundation EPSCoR program (OIA-1655280) to Auburn University. Computer resources were provided by NASA Advanced Supercomputing (NAS) Division. Lei Cheng thanks Dr. Zhifang Guo for helpful discussions. The numerical data used for generating the presented figures are available online (via 10.6084/m9.figshare.8309633).

References

Anderson, R., Harvey, C., Hoppe, M., Tsurutani, B., Eastman, T., & Etcheto, J. (1982). Plasma waves near the magnetopause. *Journal of Geophysical Research*, *87*(A4), 2087–2107.

Angelopoulos, V., Chapman, J., Mozer, F., Scudder, J., Russell, C., Tsuruda, K., et al. (2002). Plasma sheet electromagnetic power generation and its dissipation along auroral field lines. *Journal of Geophysical Research*, *107*(A8), 1181. https://doi.org/10.1029/2001JA900136

Angelopoulos, V., Kennel, C., Coroniti, F., Pellat, R., Kivelson, M., Walker, R., et al. (1994). Statistical characteristics of bursty bulk flow events. *Journal of Geophysical Research*, *99*(A11), 21,257–21,280.

Angelopoulos, V., McFadden, J. P., Larson, D., Carlson, C. W., Mende, S. B., Frey, H., et al. (2008). Tail reconnection triggering substorm onset. *Science*, *321*(5891), 931–935.

Barnes, A., & Hollweg, J. V. (1974). Large-amplitude hydromagnetic waves. *Journal of Geophysical Research*, *79*(16), 2302–2318.

Belcher, J., Davis, L., & Smith, E. (1969). Large-amplitude Alfvén waves in the interplanetary medium: Mariner 5. *Journal of Geophysical Research*, *74*(9), 2302–2308.

Chaston, C., Bonnell, J., Clausen, L., & Angelopoulos, V. (2012). Correction to "Energy transport by kinetic-scale electromagnetic waves in fast plasma sheet flows". *Journal of Geophysical Research*, *117*, A12205. https://doi.org/10.1029/2012JA018476

Chaston, C., Bonnell, J., McFadden, J., Carlson, C., Cully, C., Le Contel, O., et al. (2008). Turbulent heating and cross-field transport near the magnetopause from THEMIS. *Geophysical Research Letters*, *35*, L17S08. https://doi.org/10.1029/2008GL033601

Chaston, C., Bonnell, J. W., Wygant, J. R., Mozer, F., Bale, S. D., Kersten, K., et al. (2014). Observations of kinetic scale field line resonances. *Geophysical Research Letters*, *41*, 209–215. https://doi.org/10.1002/2013GL058507

Chaston, C., Carlson, C., Peria, W., Ergun, R., & McFadden, J. (1999). FAST observations of inertial Alfvén waves in the dayside aurora. *Geophysical Research Letters*, *26*(6), 647–650.

Chaston, C., Génot, V., Bonnell, J., Carlson, C., McFadden, J., Ergun, R., et al. (2006). Ionospheric erosion by Alfvén waves. *Journal of Geophysical Research*, *111*, A03206. https://doi.org/10.1029/2005JA011367

Chaston, C., Johnson, J., Wilber, M., Acuna, M., Goldstein, M., & Reme, H. (2009). Kinetic Alfvén wave turbulence and transport through a reconnection diffusion region. *Physical Review Letters*, *102*(1), 015001.

Chaston, C., Wilber, M., Mozer, F., Fujimoto, M., Goldstein, M., Acuna, M., et al. (2007). Mode conversion and anomalous transport in Kelvin-Helmholtz vortices and kinetic Alfvén waves at the Earth's magnetopause. *Physical Review Letters*, *99*(17), 175004.

Cheng, C., & Johnson, J. R. (1999). A kinetic-fluid model. *Journal of Geophysical Research*, *104*(A1), 413–427.

Dai, L. (2009). Collisionless magnetic reconnection via Alfvén eigenmodes. *Physical Review Letters*, *102*(24), 245003.

Dai, L., Wang, C., Zhang, Y., Lavraud, B., Burch, J., Pollock, C., & Torbert, R. B. (2017). Kinetic Alfvén wave explanation of the Hall fields in magnetic reconnection. *Geophysical Research Letters*, *44*, 634–640. https://doi.org/10.1002/2016GL071044

Damiano, P., Johnson, J., & Chaston, C. (2015). Ion temperature effects on magnetotail Alfvén wave propagation and electron energization. *Journal of Geophysical Research: Space Physics*, *120*, 5623–5632. https://doi.org/10.1002/2015JA021074

Damiano, P., Kim, E. H., Johnson, J., & Porazik, P. (2019). Electron energization by parallel electric fields in poloidal standing waves. *Journal of Geophysical Research: Space Physics*, *124*, 6691–6700. https://doi.org/10.1029/2019JA026849

Dobrowolny, M. (1972). Kelvin-Helmholtz instability in a high-β collisionless plasma. *The Physics of Fluids*, *15*(12), 2263–2270.

Dobrowolny, M. (1977). Velocity shear instability of Alfvén waves in a high β collisionless plasma. *The Physics of Fluids*, *20*(6), 1027–1028.

Duan, S., Dai, L., Wang, C., Liang, J., Lui, A., Chen, L., et al. (2016). Evidence of kinetic Alfvén eigenmode in the near-Earth magnetotail during substorm expansion phase. *Journal of Geophysical Research: Space Physics*, *121*, 4316–4330. https://doi.org/10.1002/2016JA022431

Dubinin, E., Israelevich, P., & Nikolaeva, N. (1990). Auroral electromagnetic disturbances at an altitude of 900 km: The relationship between the electric and magnetic field variations. *Planetary and Space Science*, *38*(1), 97–108.

Gershman, D. J., Adolfo, F., Dorelli, J. C., Boardsen, S. A., Avanov, L. A., Bellan, P. M., et al. (2017). Wave-particle energy exchange directly observed in a kinetic Alfvén-branch wave. *Nature Communications*, *8*, 14719.

Goertz, C. (1984). Kinetic Alfvén waves on auroral field lines. *Planetary and Space Science*, *32*(11), 1387–1392.

Goertz, C., & Boswell, R. (1979). Magnetosphere-ionosphere coupling. *Journal of Geophysical Research*, *84*(A12), 7239–7246.

Greenwald, R., & Walker, A. (1980). Energetics of long period resonant hydromagnetic waves. *Geophysical Research Letters*, *7*(10), 745–748.

Guo, Z., Hong, M., Lin, Y., Du, A., Wang, X., Wu, M., & Lu, Q. (2015). Generation of kinetic Alfven waves in the high-latitude near-Earth magnetotail: A global hybrid simulation. *Physics of Plasmas*, *22*(2), 022117.

Hasegawa, A. (1976). Kinetic theory of MHD instabilities in a nonuniform plasma. *Solar Physics*, *47*(1), 325–330.

Hasegawa, A., & Chen, L. (1976). Kinetic processes in plasma heating by resonant mode conversion of Alfvén wave. *The Physics of Fluids*, *19*(12), 1924–1934.

Hong, M., Swift, D., & Lin, Y. (2008). Ion dynamics associated with Alfven wave in the near-Earth magnetotail: Two-dimensional global hybrid simulation. *Advances in Space Research*, *41*(8), 1298–1304.

Huang, G. L., Wang, D. Y., Wu, D. J., De Feraudy, H., Le Quéau, D., Volwerk, M., & Holback, B. (1997). The eigenmode of solitary kinetic Alfvén waves observed by Freja satellite. *Journal of Geophysical Research*, *102*(A4), 7217–7224.

Hudson, P. (1971). Rotational discontinuities in an anisotropic plasma. *Planetary and Space Science*, *19*(12), 1693–1699.

Johnson, J. R., & Cheng, C. (1997). Kinetic Alfvén waves and plasma transport at the magnetopause. *Geophysical Research Letters*, *24*(11), 1423–1426.

Keiling, A. (2009). Alfvén waves and their roles in the dynamics of the Earth's magnetotail: A review. *Space Science Reviews*, *142*(1-4), 73–156.

Keiling, A., Angelopoulos, V., Runov, A., Weygand, J., Apatenkov, S., Mende, S., et al. (2009). Substorm current wedge driven by plasma flow vortices: THEMIS observations. *Journal of Geophysical Research*, *114*, A00C22. https://doi.org/10.1029/2009JA014114

Keiling, A., Wygant, J., Cattell, C., Temerin, M., Mozer, F., Kletzing, C., et al. (2000). Large Alfvén wave power in the plasma sheet boundary layer during the expansion phase of substorms. *Geophysical Research Letters*, *27*(19), 3169–3172.

Krall, N. A., & Trivelpiece, A. W. (1973). Principles of plasma physics. *American Journal of Physics*, *41*(12), 1380–1381.

Leamon, R. J., Smith, C. W., Ness, N. F., Matthaeus, W. H., & Wong, H. K. (1998). Observational constraints on the dynamics of the interplanetary magnetic field dissipation range. *Journal of Geophysical Research*, *103*(A3), 4775–4787.

Lessard, M., Lund, E., Kim, H., Engebretson, M., & Hayashi, K. (2011). Pi1B pulsations as a possible driver of Alfvénic aurora at substorm onset. *Journal of Geophysical Research*, *116*, A06203. https://doi.org/10.1029/2010JA015776

Liang, J., Lin, Y., Johnson, J. R., Wang, X., & Wang, Z. X. (2016). Kinetic Alfvén waves in three-dimensional magnetic reconnection. *Journal of Geophysical Research: Space Physics*, *121*, 6526–6548. https://doi.org/10.1002/2016JA022505

Liang, J., Lin, Y., Johnson, J. R., Wang, Z. X., & Wang, X. (2017). Ion acceleration and heating by kinetic Alfvén waves associated with magnetic reconnection. *Physics of Plasmas*, *24*(10), 102110.

Lin, Y., Johnson, J., & Wang, X. (2010). Hybrid simulation of mode conversion at the magnetopause. *Journal of Geophysical Research*, *115*, A04208. https://doi.org/10.1029/2009JA014524

Lin, Y., Johnson, J. R., & Wang, X. (2012). Three-dimensional mode conversion associated with kinetic Alfvén waves. *Physical Review Letters*, *109*(12), 125003.

Lin, Y., & Swift, D. (2002). Generation of near-Earth reconnection by divergent flows in the plasma sheet. *Journal of Geophysical Research*, *107*(A11), 1373. https://doi.org/10.1029/2002JA009308

Lin, Y., & Wang, X. (2005). Three-dimensional global hybrid simulation of dayside dynamics associated with the quasi-parallel bow shock. *Journal of Geophysical Research*, *110*, A12216. https://doi.org/10.1029/2005JA011243

Lin, Y., Wang, X., Lu, S., Perez, J., & Lu, Q. (2014). Investigation of storm time magnetotail and ion injection using three-dimensional global hybrid simulation. *Journal of Geophysical Research: Space Physics*, *119*, 7413–7432. https://doi.org/10.1002/2014JA020005

Lin, Y., Wing, S., Johnson, J. R., Wang, X., Perez, J. D., & Cheng, L. (2017). Formation and transport of entropy structures in the magnetotail simulated with a 3-D global hybrid code. *Geophysical Research Letters*, *44*, 5892–5899. https://doi.org/10.1002/2017GL073957

Lu, S., Lin, Y., Lu, Q., Wang, X., Wang, R., Huang, C., et al. (2015). Evolution of flux ropes in the magnetotail: A three-dimensional global hybrid simulation. *Physics of Plasmas*, *22*(5), 052901.

Lui, A. (2009). Comment on "tail reconnection triggering substorm onset". *Science*, *324*(5933), 1391–1391.

Lysak, R. L., & Lotko, W. (1996). On the kinetic dispersion relation for shear Alfvén waves. *Journal of Geophysical Research*, *101*(A3), 5085–5094.

Lysak, R. L., Song, Y., Sciffer, M., & Waters, C. (2015). Propagation of Pi2 pulsations in a dipole model of the magnetosphere. *Journal of Geophysical Research: Space Physics*, *120*, 355–367. https://doi.org/10.1002/2014JA020625

Osaki, H., Takahashi, K., Fukunishi, H., Nagatsuma, T., Oya, H., Matsuoka, A., & Milling, D. K. (1998). Pi2 pulsations observed from the Akebono satellite in the plasmasphere. *Journal of Geophysical Research*, *103*(A8), 17,605–17,615.

Raeder, J., Walker, R., & Ashour-Abdalla, M. (1995). The structure of the distant geomagnetic tail during long periods of northward IMF. *Geophysical Research Letters*, *22*(4), 349–352.

Shay, M., Drake, J., Eastwood, J., & Phan, T. (2011). Super-Alfvénic propagation of substorm reconnection signatures and Poynting flux. *Physical Review Letters*, *107*(6), 065001.

Shi, F., Cheng, L., Lin, Y., & Wang, X. (2017). Foreshock wave interaction with the magnetopause: Signatures of mode conversion. *Journal of Geophysical Research: Space Physics*, *122*, 7057–7076. https://doi.org/10.1002/2016JA023114

Shi, F., Lin, Y., & Wang, X. (2013). Global hybrid simulation of mode conversion at the dayside magnetopause. *Journal of Geophysical Research: Space Physics*, *118*, 6176–6187. https://doi.org/10.1002/jgra.50587

Sigsbee, K., Cattell, C., Fairfield, D., Tsuruda, K., & Kokubun, S. (2002). Geotail observations of low-frequency waves and high-speed earthward flows during substorm onsets in the near magnetotail from 10 to 13 RE. *Journal of Geophysical Research*, *107*(A7), 1141. https://doi.org/10.1029/2001JA000166

Stawarz, J., Eastwood, J., Varsani, A., Ergun, R., Shay, M., Nakamura, R., et al. (2017). Magnetospheric Multiscale analysis of intense field-aligned Poynting flux near the Earth's plasma sheet boundary. *Geophysical Research Letters*, *44*, 7106–7113. https://doi.org/10.1002/2017GL073685

Sun, W., Fu, S., Parks, G., Liu, J., Yao, Z., Shi, Q., et al. (2013). Field-aligned currents associated with dipolarization fronts. *Geophysical Research Letters*, *40*, 4503–4508. https://doi.org/10.1002/grl.50902

Swift, D. W. (1996). Use of a hybrid code for global-scale plasma simulation. *Journal of Computational Physics*, *126*(1), 109–121.

Swift, D. W., & Lin, Y. (2001). Substorm onset viewed by a two-dimensional, global-scale hybrid code. *Journal of Atmospheric and Solar-Terrestrial Physics*, *63*(7), 683–704.

Takahashi, K., Kokubun, S., Sakurai, T., McEntire, R., Potemra, T., & Lopez, R. (1988). AMPTE/CCE observations of substorm-associated standing Alfvén waves in the midnight sector. *Geophysical Research Letters*, *15*(11), 1287–1290.

Tan, B., Lin, Y., Perez, J., & Wang, X. (2011). Global-scale hybrid simulation of dayside magnetic reconnection under southward IMF: Structure and evolution of reconnection. *Journal of Geophysical Research*, *116*, A02206. https://doi.org/10.1029/2010JA015580

Temerin, M., & Roth, I. (1986). Ion heating by waves with frequencies below the ion gyrofrequency. *Geophysical Research Letters*, *13*(11), 1109–1112.

Vásconez, C., Pucci, F., Valentini, F., Servidio, S., Matthaeus, W., & Malara, F. (2015). Kinetic Alfvén wave generation by large-scale phase mixing. *The Astrophysical Journal*, *815*(1), 7.

Walén, C. (1944). On the theory of sunspots. *Arkiv for Astronomi*, *30*, 1–87.

Wang, X., Liu, Z., Li, Z., & Zhang, X. (1998). Kinetic Alfvén waves driven by velocity shear. *Physics of Plasmas*, *5*(4), 836–840.

Wygant, J., Keiling, A., Cattell, C., Johnson, l. M., Lysak, R., Temerin, M., et al. (2000). Polar spacecraft based comparisons of intense electric fields and Poynting flux near and within the plasma sheet-tail lobe boundary to UVI images: An energy source for the aurora. *Journal of Geophysical Research*, *105*(A8), 18,675–18,692.

Wygant, J., Keiling, A., Cattell, C., Lysak, R., Temerin, M., Mozer, F., et al. (2002). Evidence for kinetic Alfvén waves and parallel electron energization at 4–6 RE altitudes in the plasma sheet boundary layer. *Journal of Geophysical Research*, *107*(A8), 1201. https://doi.org/10.1029/2001JA900113